

Self-resonance preheating in deformed attractor models: oscillon formation and evolution

Bao-Min Gu,^{1,2} Yu-Peng Zhang,^{3,4,*} Fu-Wen Shu,^{1,2,†} and Yu-Xiao Liu^{3,4,‡}

¹*Department of physics, Nanchang University, Nanchang 330031, China*

²*Center for Relativistic Astrophysics and High Energy Physics, Nanchang University, Nanchang, 330031, China*

³*Key Laboratory of Quantum Theory and Applications of MoE, Lanzhou Center for Theoretical Physics, Key Laboratory of Theoretical Physics of Gansu Province,*

Gansu Provincial Research Center for Basic Disciplines of Quantum Physics, Lanzhou University, Lanzhou 730000, China

⁴*Institute of Theoretical Physics, & Research Center of Gravitation, Lanzhou University, Lanzhou 730000, China*

It is well known that, in potentials that are quadratic near the minimum but shallower away—such as small- α ($\ll M_P^2$) attractors, the inflaton condensate fragments into localized compact objects known as oscillons during self-resonance preheating. In this work we investigate the self-resonance in deformed α -attractor T-model with a Gaussian feature near the minimum, distant from inflation's end. Linear analysis reveals altered resonance bands and deformed Floquet charts dependent on feature parameters. In fully nonlinear lattice simulations, we find that the gradient energy transfer is largely independent of the potential feature parameter h . In contrast, after resonance terminates, the subsequent evolution of gradient energy becomes strongly dependent on h . Statistical analysis reveals that models with the potential feature produce larger number of smaller oscillons, with a reduced energy stored in these objects, increasingly suppressed as the magnitude of h grows. By tracking the total energy and the gradient energy contained in oscillons, we find that in models with nonzero h oscillons are systematically shorter-lived, with this effect strengthening for larger h . The gravitational wave emission is dominated by the resonant stage and becomes strongly suppressed after oscillon formation. We further find an enhancement in the high-frequency tail of the spectrum, sourced by the potential feature. Although a complete reheating description requires external couplings and higher-resolution simulations, clear qualitative differences of cosmic expansion history already emerge within our simulated time window. These results highlight the important role of potential features in shaping reheating dynamics and their cosmological implications, and provide a deeper understanding of preheating dynamics and the properties of oscillons.

I. INTRODUCTION

Inflationary cosmology [1–5] has emerged as a compelling framework for the origin of the universe and has achieved remarkable success to date. Although a direct detection of primordial gravitational waves—the definitive smoking-gun signature of inflation—remains elusive, the paradigm is strongly supported by a broad range of observations and is widely regarded as the standard cosmological scenario. In addition to resolving several conceptual shortcomings of the conventional hot Big Bang model, inflation predicts quantum vacuum fluctuations that naturally account for the small-scale anisotropies observed in the cosmic microwave background and provide the primordial seeds for large-scale structure formation in the late universe. Recent observations from the Planck satellite [6, 7] and the Atacama Cosmology Telescope (ACT) [8, 9] offer strong and independent support for the inflationary paradigm.

Inflation posits that the early universe underwent a phase of quasi-exponential expansion, which in its simplest realization can be described by a canonical single scalar field minimally coupled to gravity within gen-

eral relativity. During inflation, the inflaton field slowly rolls from a relatively flat region of its potential toward the potential minimum. Throughout this phase, the energy density of the universe is dominated by the inflaton potential, yielding an equation-of-state (EoS) parameter close to -1 , analogous to the accelerated expansion driven by dark energy of the present universe. To successfully transition to the subsequent radiation dominated era and enable Big-Bang nucleosynthesis (BBN), the energy stored in the inflaton potential must be transferred to relativistic particles through an intermediate stage known as reheating.

Early studies proposed perturbative decay as the mechanism for reheating [10–12]. However, this description is valid only in the regime of weak couplings and, moreover, violates the fluctuation dissipation theorem [13, 14]. Consequently, perturbative decay alone is now understood to be insufficient for a complete description of the reheating process, which is highly non-perturbative. In contrast, the subsequently proposed mechanism of parametric resonance provides a more natural and successful description of particle production [15–17]. In the presence of external coupling(s), the matter field(s) remains negligible in the initial stage of parametric resonance and the inflaton undergoes coherent oscillations with decaying amplitude around the minimum of its potential. During the inflaton oscillations, the Fourier modes of the matter fields experience a time-dependent

* zhangyupeng@lzu.edu.cn; Contact author.

† shufuwen@ncu.edu.cn; Contact author.

‡ liuyx@lzu.edu.cn; Contact author.

effective frequency induced by their coupling to the inflaton. For suitable inflaton dynamics and model parameters, the evolution of this effective frequency violates the adiabaticity condition, leading to exponential amplification of the matter field modes and consequently, explosive particle production. Once the occupation number of the matter field grows sufficiently large, its backreaction on the background becomes important and eventually shuts off the resonance. Interestingly, preheating can occur even in the absence of external couplings. In this case however, the inflaton does not decay into new particle species; instead, the inflaton transfers energy into its own fluctuations through nonlinear self-interactions, resulting in the formation of spatially localized, dense, and long-lived oscillons [18–21]. This mechanism is known as self-resonance. For reviews on reheating process, see references [22–25].

In recent years, it has been established that oscillon formation requires the inflationary potential to satisfy certain conditions: it should be approximately quadratic around the minimum, while becoming shallower than quadratic away from the minimum; including gravitational effects would further enhance the formation efficiency [26, 27]. It has been demonstrated that a broad class of inflationary models, such as monodromy inflation [21, 28–30], string-inspired models [31–33], α -attractors [32, 34–37], hilltop [38, 39], and non-canonical scenarios [40, 41], can give rise to oscillon formation. Since oscillon formation and their characteristic properties vary among different models, studying oscillon would provide valuable insight into the dynamics of the reheating process of these models. Oscillons are soliton-like, non-topological defect configurations that are not protected by any symmetry and are therefore metastable. Nevertheless, their lifetimes can be extremely long. Oscillons have attracted broad interest for several reasons. In cosmology, oscillons behave effectively as non-relativistic matter with EoS close to zero, hence they decay slower than radiation. In preheating process, the copious production of oscillons during preheating can drive the universe into a transient early matter-dominated (eMD) phase, provided that their lifetimes are sufficiently long. Such an eMD phase would have significant impact on the expansion history of the universe and thus the inflationary observable [42–45]. Moreover, because oscillons are spatially localized configurations, they carry considerable gradient energy with spatial anisotropies. The formation and decay of oscillons may act as efficient source for the generation of stochastic gravitational wave background [28, 46–57]. Recent studies have further suggested that oscillons may collapse into primordial black holes (PBHs) [26, 58–63]. If sufficiently long-lived, oscillons may also constitute viable dark matter candidates [64, 65]. In field theory and particle physics, oscillons provide a paradigmatic example of long-lived, localized excitation in strongly nonlinear, non-equilibrium field theories, offering insights into energy localization, slow thermalization, and the emergence

of effective particle-like degrees of freedom across high-energy, nonlinear, and condensed-matter physics [66–69]. These considerations motivated widespread interest in studying the formation mechanism and dynamical properties of oscillons, such as shape, decay, and lifetime [20, 35, 39, 70–87].

In this paper, we study the preheating process realized by self-resonance of deformed T-model α -attractors. The model composed of a standard T-model potential with an additional Gaussian-type feature. As an exploratory study, this work is motivated by two main aspects. First, inflationary models with features in the potential have attracted growing interest, as they naturally lead to rich and nontrivial cosmological dynamics. In particular, suitably chosen features during inflation can substantially enhance curvature perturbations, opening a viable window for PBH production [88–100]. Different classes of features can generate PBHs across a broad mass range, from asteroid masses to stellar scales, with correspondingly distinct mass functions and abundances. While current observational bounds severely constrain scenarios in which PBHs make up the entirety of dark matter [101–110], PBHs remain viable as a subdominant dark matter component and as possible progenitors of black holes involved in certain compact binary mergers [111–118]. Motivated by these considerations, we undertake an exploratory study of the consequences of placing the potential feature in the post-inflationary reheating phase rather than during inflation, and investigate how it affects the details of the reheating process, including its dynamics and energy transfer. Reheating dynamics in the presence of features in the potential were previously studied in reference [119], where a quadratic base potential supplemented by a quadratic-quadratic type of inflaton-daughter coupling was considered. It was shown that the reheating process can be substantially modified, leading to a number of nontrivial and interesting results; for details, we refer the readers to reference [119]. The second motivation of this work is related to oscillon physics. Despite the new constraints from the latest ACT observations [8, 9], α -attractors models remain an attractive and well-motivated class of inflationary theories. Previous studies have shown that oscillon formation during reheating occurs for small α , but is absent for large α [120, 121]. In this work, we concentrate on the small- α regime and explore how the potential features affect oscillon formation and their subsequent dynamics. We expect that the introduced feature in the potential, together with its associated parameters, can play the role of probe parameters—analogue to test particles in spacetime—thereby providing insight into the detailed dynamics of oscillon formation.

This paper is organized as follows. In section II, we present the inflationary dynamics and introduce the deformed T-model together with the model setup. In section III, we investigate parametric resonance within the framework of linear perturbation theory. In particular we show the results of Floquet analysis. In section IV, we

show the main results of this paper, including the lattice simulations, the oscillon dynamics and properties, and a brief discussion on the implication for the evolution of the universe. The conclusions and outlook are presented in section V, with supplementary appendix provided in appendix A.

II. THE INFLATIONARY DYNAMICS

To study the post-inflationary dynamics, we consider general relativity minimally coupled to a canonical scalar field, the inflaton, described by the action

$$S = \int d^4x \sqrt{-g} \left(\frac{M_P^2}{2} R - \frac{1}{2} (\partial\phi)^2 - V(\phi) \right). \quad (1)$$

We work in a spatially flat Friedmann–Robertson–Walker background,

$$ds^2 = -dt^2 + a^2(t) \delta_{ij} dx^i dx^j, \quad (2)$$

with $a(t)$ the scale factor. Under this ansatz, the background evolution then obeys

$$\ddot{\phi} + 3H\dot{\phi} + V_\phi = 0, \quad (3)$$

$$\frac{1}{2} \dot{\phi}^2 + V(\phi) = 3M_P^2 H^2, \quad (4)$$

$$-\frac{1}{2} \dot{\phi}^2 = M_P^2 \dot{H}, \quad (5)$$

where dot denotes the derivative with respect to t , $H = \dot{a}/a$ is the Hubble parameter. During slow-roll inflation, the scale factor grows exponentially and the Hubble parameter H is nearly a constant, leading to a quasi-de Sitter period of expansion. This can be realized if the slow-roll parameters are small, i.e.,

$$\epsilon \equiv -\frac{\dot{H}}{H^2} \simeq \epsilon_V \equiv \frac{1}{2} M_P^2 \left(\frac{V_\phi}{V} \right)^2 \ll 1, \quad (6)$$

$$\eta \equiv \frac{\ddot{\phi}}{H\dot{\phi}} \simeq \eta_V \equiv \frac{V_{\phi\phi}}{V} \ll 1. \quad (7)$$

Using the slow-roll parameter ϵ_V , the duration of inflation can be calculated by

$$N_{\text{tot}} = \int_{t_e}^{t_*} H dt \simeq \int_{\phi_e}^{\phi_*} \frac{d\phi}{\sqrt{\epsilon_V}}, \quad (8)$$

where the subscripts “*” and “e” marks the horizon exit of the CMB scales ($k_* = 0.05 \text{ Mpc}^{-1}$) and the end of inflation, respectively. Typically, the total duration of inflation is required to satisfy $N_{\text{tot}} \gtrsim 50$. This lower bound arises from two considerations: (i) resolving the horizon, flatness, and other puzzles of the hot big bang scenario, and (ii) satisfying the constraints on the scalar spectral index and the tensor-to-scalar ratio from CMB observations, which generally favor $N_{\text{tot}} \gtrsim 50$. In addition, the amplitude of the scalar power spectrum A_s

and the spectral index n_s are severely constrained by the CMB observations [6–9]. They are computed by

$$A_s = \frac{H_*^2}{8\pi^2 \epsilon_*} \simeq \frac{1}{12\pi^2} \frac{V^3(\phi_*)}{V_\phi^2(\phi_*)}, \quad (9)$$

$$n_s = 1 - 6\epsilon_V(\phi_*) + 2\eta_V(\phi_*). \quad (10)$$

These constraints restrict the model parameters as well as the field values at horizon exit and at the end of inflation.

The model considered in this work has the form

$$V(\phi) = V_b(\phi) \left[1 + h \exp \left(-\frac{(\phi - \phi_s)^2}{2\sigma^2} \right) \right], \quad (11)$$

where the parameters h , ϕ_s , and σ characterizes the height, the position, and the width of the feature, respectively. The potential $V_b(\phi)$ is chosen to be consistent with observations. We restrict the height h and the width σ to be small enough and the position ϕ_s to be after the end of inflation, such that the CMB observations are well described by the base potential $V_b(\phi)$. In this work we consider the T-model of α -attractors as the base potential,

$$V_b(\phi) = V_0 \tanh^2 \left(\frac{\phi}{\sqrt{6\alpha}} \right). \quad (12)$$

We show the plot of this potential in figure 1. The parameter sets used in this paper are listed in table I. They are in good agreement with latest observational constraints, as can be seen in appendix A.

III. PERTURBATIVE APPROACH OF PREHEATING

A. Perturbative equations

We first study the self-resonance perturbatively. The inflaton field can be decomposed into a combination of homogeneous background field and a fluctuation part, $\phi(t, \vec{x}) = \phi(t) + \delta\phi(t, \vec{x})$. The homogeneous field $\phi(t)$ obeys equation (3). The fluctuation part can be analyzed more conveniently in Fourier space, by expanding it as

$$\delta\phi(t, \vec{x}) = \int \frac{d^3k}{(2\pi)^3} \delta\phi_k(t) e^{-i\vec{k}\cdot\vec{x}}. \quad (13)$$

The Fourier mode $\delta\phi_k(t)$ then satisfies

$$\delta\ddot{\phi}_k + 3H\delta\dot{\phi}_k + \left(\frac{k^2}{a^2} + V''(\phi(t)) \right) \delta\phi_k = 0, \quad (14)$$

where $V''(\phi(t)) = \partial^2 V(\phi(t))/\partial\phi(t)^2$. Note that the metric perturbations are neglected. During the early stages of preheating, the fluctuation $\delta\phi(t, \vec{x})$ remains small, i.e. $\delta\phi(t, \vec{x}) \ll \phi(t)$. The dynamics of preheating can be well described by equation (14). As preheating proceeds, the energy of the inflaton field is continuously

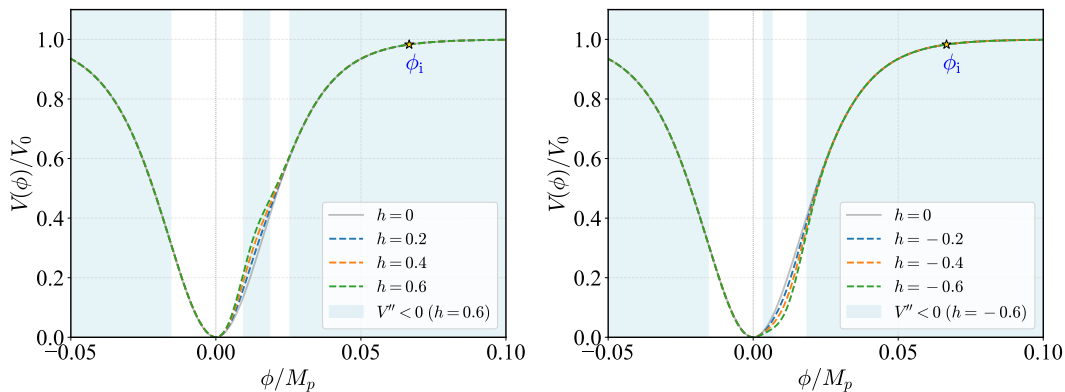


FIG. 1. Plots of the deformed T-model potential for the parameters in table I. The end of inflation ϕ_i is defined by $\epsilon_V(\phi_i) = 1$. The blue shaded regions are those with $V'' < 0$ indicating the field space where tachyonic instability may occur.

Sets	$V_0 [M_p^4]$	$\alpha [M_p^2]$	h	$\sigma [M_p]$	$\phi_s [M_p]$
P_0	1.14×10^{-14}	10^{-4}	0	6×10^{-3}	8×10^{-3}
P_1	1.14×10^{-14}	10^{-4}	$0 < h \leq 0.6$	6×10^{-3}	8×10^{-3}
P_2	1.14×10^{-14}	10^{-4}	$-0.6 \leq h < 0$	6×10^{-3}	8×10^{-3}

TABLE I. The parameter sets used in this paper. In the main text, we focus on the feature amplitude h , while the effects of the width and position parameters are briefly discussed in the appendix.

transferred to the fluctuation modes, which—under suitable conditions—can be resonantly amplified. Once the fluctuations are amplified to amplitudes comparable to the background, the perturbative expansion would break-down and the backreaction becomes important. At this stage, equation (14) no longer provides an accurate description of preheating, which must instead be studied by fully nonlinear methods. Nevertheless, in this section we employ a perturbative approach to gain qualitative insight into the dynamics of preheating, while a more precise and detailed nonlinear analysis will be presented in section IV.

B. Floquet analysis

Equation (14) describes the evolution of $\delta\phi_k(t)$ with a time-dependent frequency defined by

$$\omega_k^2(t) = \frac{k^2}{a^2} + V''(\phi(t)). \quad (15)$$

Self-resonance arises when the fluctuation modes $\delta\phi_k(t)$ exhibit exponential growth over a broad range of wavenumbers. This phenomenon can be triggered by distinct mechanisms, most notably parametric resonance and tachyonic preheating. Parametric resonance occurs when the adiabaticity condition is violated, $|\dot{\omega}(t)/\omega^2(t)| > 1$, signaling the breakdown of the WKB approximation [15, 17]. Tachyonic preheating, on the other hand, takes place when the inflaton traverses a region of the potential with negative effective mass squared,

i.e., $\omega^2(t) < 0$ [17, 122]. This behavior occurs in certain inflationary models, such as the hybrid inflation [123] and α -attractors [124, 125]. In figure 2, it is evident that both parametric resonance and tachyonic instability coexist in the model under consideration.

Now let us study the solutions of equation (14) in detail. According to the Floquet theorem [126], the general solution of $\delta\phi_k(t)$ can be given by

$$\delta\phi_k(t) = P_+(t)e^{\mu_k t} + P_-(t)e^{-\mu_k t}, \quad (16)$$

where $P_{\pm}(t)$ are periodic functions with the frequency determined by $\partial^2 V(\phi(t))/\partial\phi^2$. This can be understood by Taylor expanding the potential around the minimum and neglecting the terms higher than quadratic order of $\delta\phi$. The remaining mass term explains the oscillation nature of $P_{\pm}(t)$. The parameter μ_k is the Floquet exponent, which characterizes the growth rate of the fluctuations. For imaginary μ_k , the fluctuation $\delta\phi_k$ simply oscillates periodically and there is no instability. For $\Re(\mu_k) > 0$, however, the corresponding fluctuation mode grows exponentially. The continuously distributed modes form instability bands in parameter space. The resonance is efficient if $\Re(\mu_k)/H \gg 1$, for which a significant fraction of the inflaton energy is transferred into fluctuations. In general, the Floquet exponent μ_k can be evaluated numerically. The details are given in appendix B.

We show the Floquet exponents of the deformed T-model in figure 3. Clearly, the upper two rows of figure 3 show that the instability bands are deformed compared to the original T-model. We find that positive h (P_1 set) modifies the strongest broad resonance band of the original T-model, creating a new resonance region in the

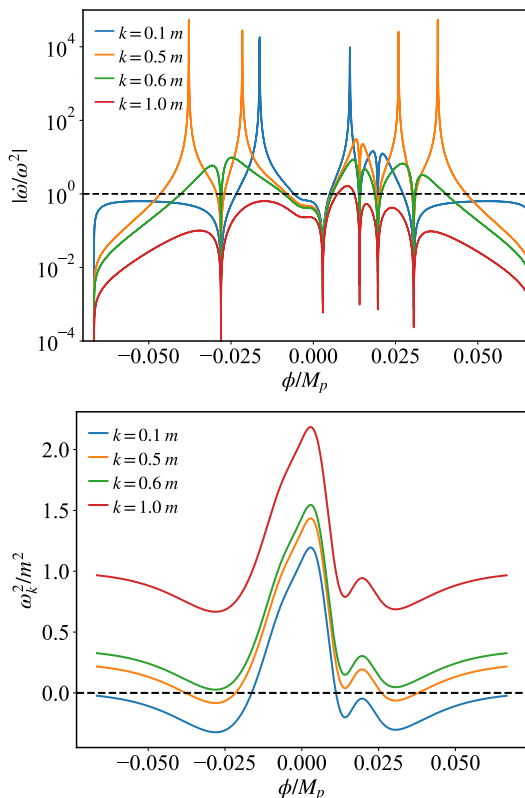


FIG. 2. The violation of adiabatic condition for parametric resonance and the tachyonic instability condition for deformed T-model ($h = 0.2$).

field range around the potential feature. Negative values of h slightly narrows the field-space region in which broad resonance occurs, but the slightly higher broad resonance band implies that more high-momentum fluctuation modes can be excited in resonance. A very narrow additional instability band appears near the potential feature. Its extent is highly limited, affecting only modes with $k \lesssim 0.5m$ as the inflaton crosses the feature, and the associated Floquet exponents remain smaller than those of the primary band. All these effects scale positively with the magnitude of h . We also show the Floquet exponents for fixed mode and field value in figure 3. We find that the resonance efficiency of low-momentum modes is enhanced to varying degrees. The enhancement is more pronounced for models with $h > 0$, while it is relatively weaker for models with $h < 0$.

IV. NON-PERTURBATIVE DYNAMICS OF PREHEATING: LATTICE SIMULATION

A. Setup and initialization

As noted above, perturbative analyses based on equation (14) are inherently limited: once fluctuations grow large enough, the expansion ceases to be valid and non-

linear effects dominate, rendering perturbative predictions unreliable. In this regime, equations (3)–(5) together with equation (14) are no longer applicable, and the scalar field dynamics must instead be governed by the following nonlinear equations:

$$\ddot{\phi} + 3H\dot{\phi} - \frac{1}{a^2}\nabla^2\phi + V_\phi = 0, \quad (17)$$

$$\frac{1}{2}\dot{\phi}^2 + \frac{1}{2a^2}(\nabla\phi)^2 + V = 3M_P^2H^2, \quad (18)$$

where $\phi = \phi(t, \vec{x})$ and ∇ is the spatial gradient operator.

In this section, we use the publicly available code *CosmoLattice* [127–129] to study preheating from a fully nonlinear, lattice-based perspective. *CosmoLattice* evolves a system within a finite discretized box using dimensionless quantities, such as model parameters, fields, and the potentials. For this purpose, all quantities must first be rescaled to dimensionless form, which we achieve by introducing a set of scaling parameters (m, ϕ_i), with m being the inflaton mass defined by $m^2 = \left. \frac{\partial^2 V}{\partial \phi^2} \right|_{\phi=0}$ and ϕ_i the field value at the end of inflation marking the onset of preheating. The coordinates and fields are rescaled as

$$\tilde{t} = mt, \quad \tilde{x} = mx, \quad \tilde{\phi} = \frac{\phi}{\phi_i}. \quad (19)$$

For convenience, we also use a new dimensionless parameter $\lambda = M_P/\sqrt{6\alpha}$ instead of α . With these new variables and parameters, the kinetic, gradient, and potential energies are rescaled to be

$$\tilde{E}_K = \frac{1}{m^2\phi_i^2} \frac{1}{2}\dot{\phi}^2 = \frac{1}{2}(\partial_{\tilde{t}}\tilde{\phi})^2, \quad (20)$$

$$\tilde{E}_G = \frac{1}{m^2\phi_i^2} \frac{1}{2}\left(\frac{\nabla\phi}{a}\right)^2 = \frac{1}{2}\left(\frac{\tilde{\nabla}\tilde{\phi}}{a}\right)^2, \quad (21)$$

$$\tilde{V} = \frac{1}{m^2\phi_i^2}V(\phi) = \frac{M_p^2}{2\lambda^2\phi_i^2}\tanh^2\left(\lambda\frac{\phi_i}{M_p}\tilde{\phi}\right) \times \left\{1 + h \exp\left[-\frac{\phi_i^2}{2\sigma^2}\left(\tilde{\phi} - \frac{\phi_s}{\phi_i}\right)^2\right]\right\}, \quad (22)$$

where $\tilde{\nabla} = \nabla/m$. Accordingly, the rescaled energy density and pressure are

$$\tilde{\rho} = \frac{1}{m^2\phi_i^2}\rho = \tilde{E}_K + \tilde{E}_G + \tilde{V}, \quad (24)$$

$$\tilde{p} = \frac{1}{m^2\phi_i^2}p = \tilde{E}_K - \frac{1}{3}\tilde{E}_G - \tilde{V}. \quad (25)$$

In *CosmoLattice*, we evolve the dimensionless version of equations (17) and (18),

$$\partial_{\tilde{t}}^2\tilde{\phi} + 3\tilde{H}\partial_{\tilde{t}}\tilde{\phi} - \frac{1}{a^2}\tilde{\nabla}^2\tilde{\phi} + \tilde{V}_{\tilde{\phi}} = 0, \quad (26)$$

$$\frac{1}{2}(\partial_{\tilde{t}}\tilde{\phi})^2 + \frac{1}{2a^2}(\tilde{\nabla}\tilde{\phi})^2 + \tilde{V} = 3\frac{M_P^2}{\phi_i^2}\tilde{H}^2, \quad (27)$$

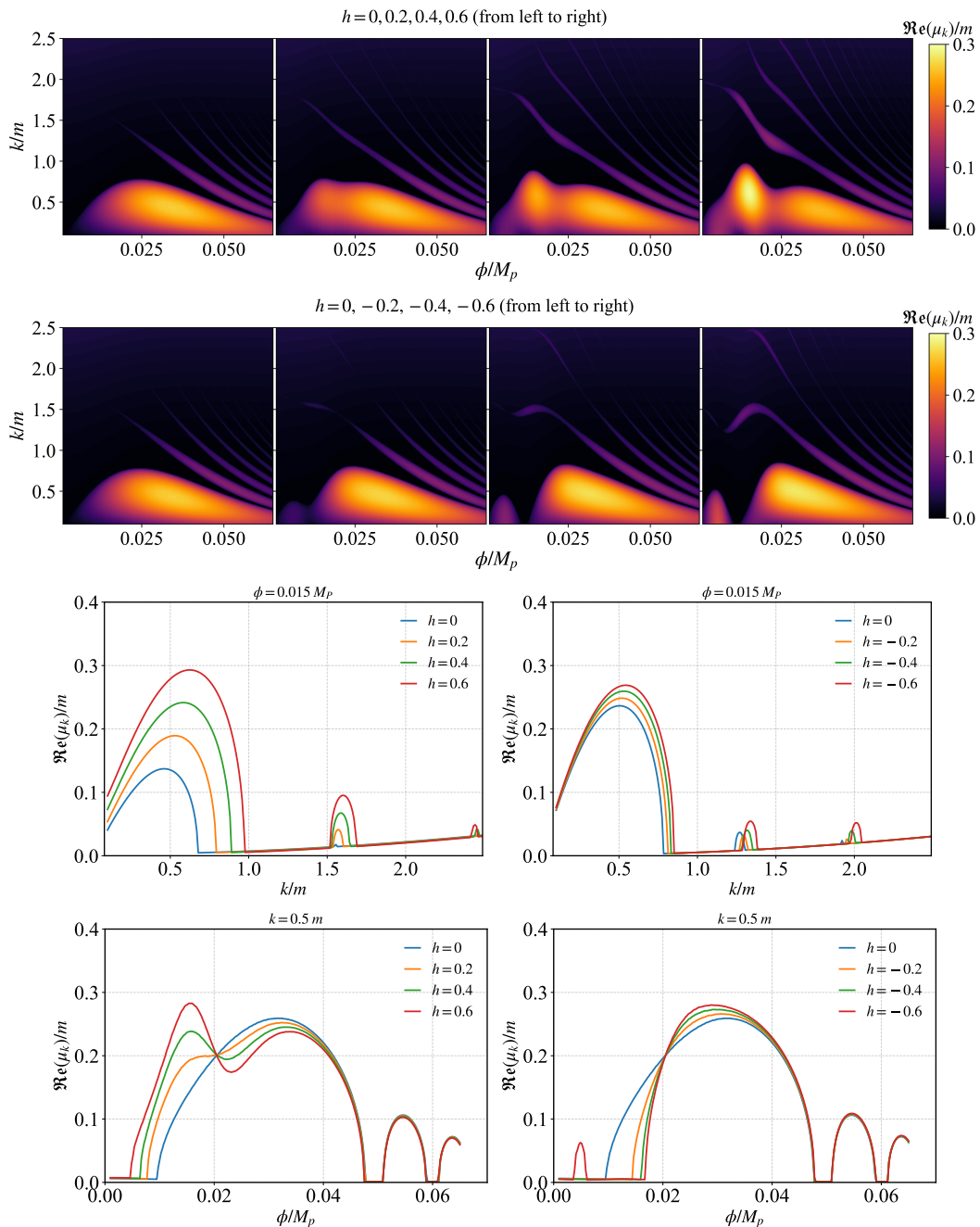


FIG. 3. *Upper two rows*: The Floquet charts for the models with P_1 and P_2 set of parameters. *Lower two rows*: The Floquet exponents of different modes evaluated at a fixed field value $\phi = 0.015 M_P$, as well as those of the mode $k = 0.5 m$ evaluated at different field values. Note that these results are obtained with cosmic expansion neglected.

where $\tilde{H} = H/m$.

To initialize the simulations, we need to impose initial conditions for equations (26) and (27). In this work, we start the simulation at $\epsilon_V = 1$, corresponding to $\phi = \phi_i$, with the initial momentum $\dot{\phi}_i$ determined numerically from the homogeneous mode equation (3). In our setup, the characteristic region of the potential lies far from ϕ_i , such that the correction term in equation (11) is exponentially suppressed. This allows us to adopt the orig-

inal T-model ($h = 0$) values of $(\phi_i, \dot{\phi}_i)$ directly for the parameter sets listed in table I. The values of the initial conditions employed in our simulations are fixed at $\phi_i = 0.06665 M_P$ with velocity $\dot{\phi}_i = -1.656 \times 10^{-8} M_P^2$. The main results presented in this work are based on simulations with $N^3 = 384^3$ grids and infrared cutoff $k_{\text{IR}} = 0.1 m$, which yields a box size $L = 20\pi m^{-1}$ and a lattice spacing $dx \approx 0.1635 m^{-1}$. The ultra-violet cut-off is $k_{\text{UV}} = \frac{\sqrt{3}}{2} N k_{\text{IR}} \approx 33 m$. The reason why we use

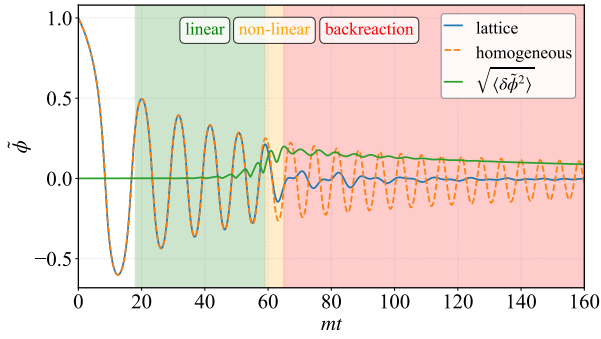


FIG. 4. Comparison of the field evolution result obtained from the nonlinear equation (26) and the homogeneous equation (3), and the r.m.s $\sqrt{\langle \delta \tilde{\phi}^2 \rangle}$ (green), for the parameter set P_1 with $h = 0.4$.

this setup are explained in the convergence test in appendix C. All lattice simulations presented are performed with second order velocity-verlet algorithm.

B. Fields and fluctuations

In this subsection we analyze the data of lattice simulations, in particular those related to oscillon formation. The output data contains averages, spectra, and snapshots. Here, the average denotes the volume average of the physical quantity over the lattice. For example, the scalar field value is given by the volume average of the scalar field at all points of the lattice,

$$\langle \tilde{\phi}(\tilde{t}, \vec{\tilde{x}}) \rangle = \frac{1}{N^3} \int_{\text{volume}} d^3 \tilde{x} \tilde{\phi}(\tilde{t}, \vec{\tilde{x}}) = \frac{1}{N^3} \sum_{\vec{\tilde{x}}} \tilde{\phi}(\tilde{t}, \vec{\tilde{x}}). \quad (28)$$

The symbol $\langle \dots \rangle$ denotes volume average. For notational simplicity, we omit this symbol in what follows, with quantities such as field values, fluctuations, and energy densities understood as the volume-averaged one.

Now let us analyze the evolution of the scalar field and its fluctuations in lattice. As an example, in figure 4 we show the comparison of field evolution obtained from the nonlinear equation (26) (the evolution of the field fluctuations for other parameter sets are shown in figure 17 in appendix) and that from the homogeneous equation (3), as well as the fluctuation, which is defined by the root mean square (r.m.s) of the scalar field,

$$\sqrt{\langle \delta \tilde{\phi}^2 \rangle} = \sqrt{\langle \tilde{\phi}^2(t, \vec{x}) \rangle - \langle \tilde{\phi}(t, \vec{x}) \rangle^2}. \quad (29)$$

We observe that the two approaches exhibit a clear discrepancy. Although they coincide in the early stage (linear regime) of preheating, once fluctuations grow to amplitudes comparable to the background field, the perturbative expansion breaks down and nonlinear effects become significant. In the nonlinear regime, fluctuations

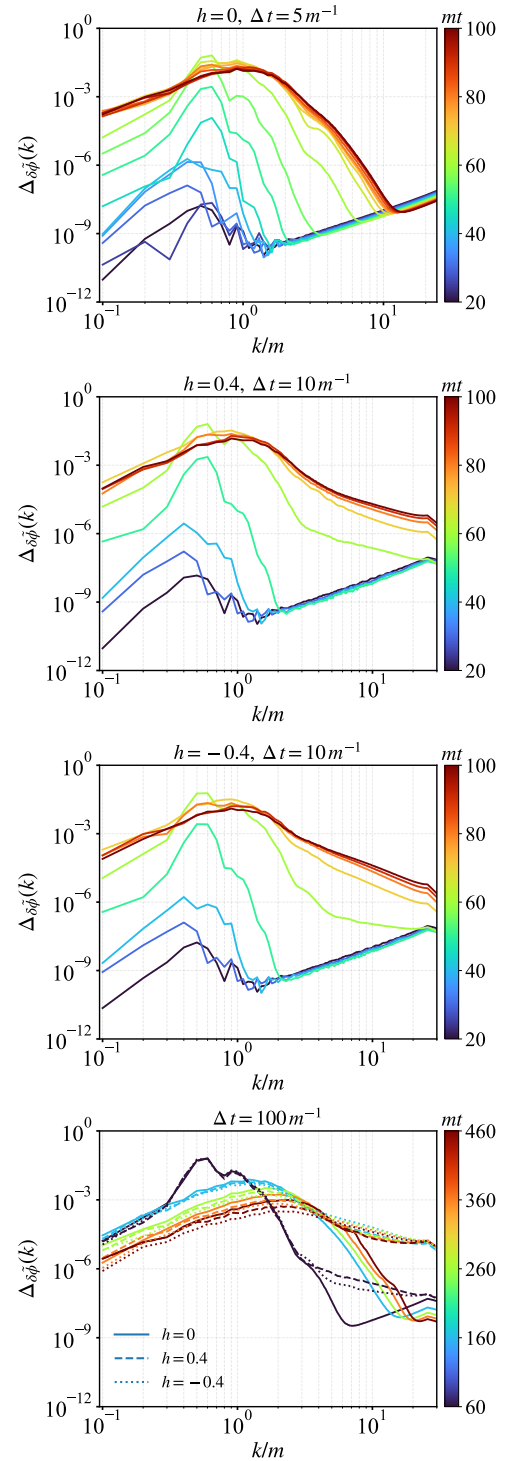


FIG. 5. Dimensionless power spectra of scalar fluctuations. The plots correspond to $h = 0$ (upper left), $h = 0.4$ (upper right), $h = -0.4$ (lower left), and the comparison of spectra.

continue to grow until they significantly affect the background evolution, at which backreaction shuts off the resonance.

Combining the evolution of the fluctuations in fig-

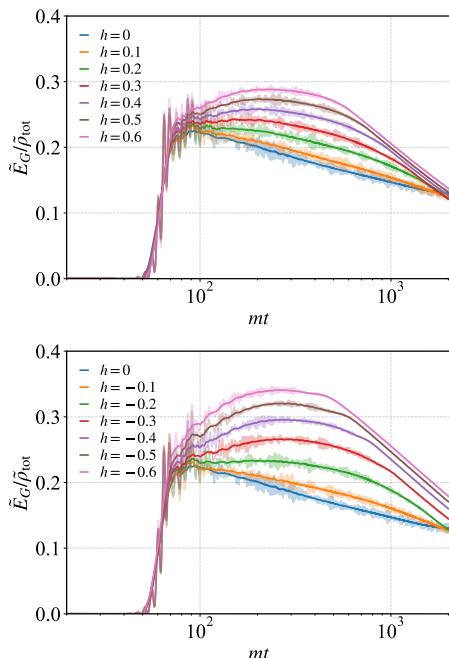


FIG. 6. The evolution of gradient energy for P_1 (left) and P_2 (right) set of parameters. The lighter curves show the raw volume-averaged fraction of gradient energy, while the darker curves represent the result after applying an oscillation-averaged smoothing procedure.

ure 17, we find that the growth of fluctuations in resonance stage is similar for all parameters. For all parameter sets, the fluctuations grow and peak within the time interval $60 m^{-1} \lesssim t \lesssim 70 m^{-1}$. Once the fluctuations peak, the subsequent backreaction stage exhibits a faster decay for $|h| \neq 0$, and the suppression becomes stronger as $|h|$ increases, hence the amplitude of fluctuations for $h \neq 0$ is slightly smaller than that of the original T -model ($h = 0$). Part of these features are likewise reflected in the power spectra 5. We see that the peak amplitudes of the power spectra are nearly identical and occur in the time interval $60 m^{-1} \lesssim t \lesssim 70 m^{-1}$. Resonant amplification first occurs for low-momentum modes and subsequently extends to higher momenta. Notably, in the $h = 0$ case the resonance is largely confined to modes with $k \lesssim 10 m$, whereas for $h \neq 0$ higher-momentum modes are also excited after the resonance stage. We thus conclude that the characteristic structures of the potential primarily influence high-momentum (small-scale) modes, and that this effect is largely confined in the backreaction stage.

C. Formation and decay of oscillons

1. gradient energy

Now let us analyze the energy transfer in preheating. During the period of self-resonance, the inflaton transfers

energy to its own fluctuations, leading to their amplification and the formation of a spatially anisotropic energy distribution. As an example, we show the fraction of the volume averaged gradient energy in figure 6. We see that the kinetic and potential energies of the inflaton field are efficiently transferred into gradient energy, leading to its exponential growth before the resonance terminates. These results reveal several characteristic features.

- The fraction of gradient energy reaches a maximum of approximately 20%-35% (for the parameters considered), the same magnitude with contributions from the kinetic and potential sectors. The peak of gradient energy fraction increases with $|h|$, and for the same $|h|$ it is larger for negative h than for positive h . hence, the presence of potential feature accelerates the fragmentation of the homogeneous inflaton mode and enhances its energy transfer.
- Across different models, the gradient energy fraction exhibits distinct behaviors at different stages. In the resonance stage ($t \lesssim 70 m^{-1}$), the growth of the gradient energy fraction is nearly identical for all models, showing no significant differences. After the resonance stage, however, clear model-dependent features emerge, with larger values of h leading to a more pronounced growth of the gradient energy fraction. In the backreaction stage, the gradient energy fraction in the $h = 0$ case decays as a power law in time, whereas for $h \neq 0$ it displays a qualitatively different evolution. For larger values of $|h|$, the gradient energy fraction undergo another period of growth, allowing it to reach a higher peak, but also decay faster. It was suggested that the decay of the total gradient energy can be employed to define the lifetime of oscillons. However, in this work, we will introduce more reliable new methods to determine the lifetime of oscillons later.
- For sufficiently large $|h| \gtrsim 0.3$, the gradient energy fraction exhibits a power-law decay in time beyond a characteristic epoch, appearing as straight lines with identical slopes, see figure 6. The onset of this regime depends on $|h|$, occurring at earlier times for larger values of $|h|$. As will be shown below, this behavior is closely related to the decay of gradient energy distributed inside and outside oscillons.

2. Properties of oscillons

It is well known that the gradient energy plays a crucial role in oscillon formation. During resonance, a significant fraction of the inflaton field energy is transferred into the fluctuations, leading to highly anisotropic spatial distribution of energy. After the resonance ends, provided that the potential has an appropriate shape—typically shallower than a quadratic form around its minimum, which induces an effective attractive self-interaction—the

anisotropic energies can coalesce into spatially localized, long-lived, non-topological solitons with oscillatory behavior, known as oscillons. In numerical simulations, the formation of oscillons is typically identified by the emergence of spatially localized overdense regions with energy densities exceeding several times of the average background value. The threshold energy density $\tilde{\rho}_{\text{th}}$ is commonly set in the range $\tilde{\rho}_{\text{th}}/\tilde{\rho}_{\text{ave}}$ between 3 and 10 [21, 28, 32], where $\tilde{\rho}_{\text{ave}}$ is the volume averaged total energy density in the box. We emphasize that different threshold criteria select different oscillon populations; consequently, the inferred oscillon properties can vary substantially depending on the adopted threshold. In this work we use the threshold energy density $\tilde{\rho}_{\text{th}} = 10\tilde{\rho}_{\text{ave}}$. Figure 7 presents the two-dimensional snapshots of the oscillon configurations for $h = 0$ and $h = \pm 0.6$, respectively. These snapshots reveal distinguishable differences among the oscillons produced under different parameter choices.

To capture the properties of oscillons, let us study the details of these overdense objects. We define the energy fraction of the overdense objects,

$$f_{\text{osc}}(\tilde{t}) = \frac{\int_{\tilde{\rho} \geq \tilde{\rho}_{\text{th}}} d^3\tilde{x} \rho(\tilde{t}, \tilde{\mathbf{x}})}{\tilde{\rho}_{\text{ave}} \times \text{volume}}. \quad (30)$$

It represents the energy fraction contained in dense objects relative to the total energy in the box. The total (comoving) volume of the dense objects \mathcal{V}_{osc} is calculated by integrating over regions with energy density above the threshold $\tilde{\rho}_{\text{th}}$. We also count the number of the objects, \mathcal{N}_{osc} , identified by the simply connected regions with energy density above the threshold ρ_{th} . Thus the total volume, the mean volume, and the energy contained per overdense object are given by

$$\mathcal{V}_{\text{osc}} = \int_{\tilde{\rho} \geq \tilde{\rho}_{\text{th}}} d^3\tilde{x}, \quad \mathcal{V}_{\text{mean}} = \frac{\mathcal{V}_{\text{osc}}}{\mathcal{N}_{\text{osc}}}, \quad (31)$$

$$\tilde{E}_p = \frac{a^3(\tilde{t})}{\mathcal{N}_{\text{osc}}} \int_{\tilde{\rho} \geq \tilde{\rho}_{\text{th}}} d^3\tilde{x} \tilde{\rho}(\tilde{t}, \tilde{\mathbf{x}}). \quad (32)$$

This allows us to define the physical size of oscillons by $R_{\text{phy}} = a(\tilde{t})(3\mathcal{V}_{\text{mean}}/4\pi)^{1/3}$. In the following, we will discuss the properties of the oscillons and the relation with the potential feature.

3. Morphology and number

We show the volume fraction, the averaged physical size, and the number of the overdense objects in figure 8. During the resonance stage, the energy of the homogeneous mode of the inflaton is continuously transferred into gradient energy, leading to a steady growth of the volume fraction of overdense regions. At the end of resonance ($t_{\text{re}} \sim 70 m^{-1}$), the comoving volume fraction of regions with densities exceeding $5\tilde{\rho}_{\text{ave}}$ reaches approximately 4.5%, while that above $10\tilde{\rho}_{\text{ave}}$ is about

1.0%, with negligible differences among models with different h . After resonance, the attractive nature of the potential further enhances these overdense regions, causing their volume fractions to increase and reach a maximum. Subsequently, due to cosmic expansion, the comoving volume fractions gradually decrease and eventually approach zero. This process exhibits a strong dependence on h , with the growth and the peak becoming increasingly suppressed as h increases. Interestingly, the peaks of the volume fractions defined by the two density thresholds do not coincide: after the volume fraction above $5\tilde{\rho}_{\text{ave}}$ (light dashed curve) reaches its maximum at $\sim 100 m^{-1}$, the fraction above $10\tilde{\rho}_{\text{ave}}$ (dark solid curve) continues to grow for a period of time. This behavior indicates that, following oscillon formation ($t_{\text{of}} \sim 100 m^{-1}$, which can also be confirmed by the energy analysis later), the oscillon cores become progressively more compact under the attractive force of the potential.

The volume fraction of dense regions is suppressed at larger $|h|$, regardless of the threshold definition. This behavior is primarily due to the reduction in the oscillon size (see the right panel of figure 8); although the number of oscillons increases compared to the $h = 0$ case, this increase is insufficient to compensate for their smaller volumes. The presence of the feature in the inflationary potential increases the number of oscillons. Taking $t_{\text{of}} = 100 m^{-1}$ as the formation time of oscillons, the oscillon number varies by at most a few times across different values of h . After formation, oscillons merge with one another, leading to a decrease in their number until a relatively stable value is reached. Subsequently, oscillon decay causes fragmentation and a corresponding increase in number. It is worth noting that in models with $|h| < 0.2$, the oscillon lifetimes are much longer than our simulation time, so their number remains approximately constant in our simulations¹, and the decay-induced increase is not observed.

We now turn to the size of oscillons. The evolution of the physical size of dense regions shows that oscillons do not form at the end of the resonance stage. At the end of resonance, the average size of each singly connected high-density region reaches a maximum, although their shapes are highly irregular (see the leftmost column of figure 7). Over the subsequent interval of about $\sim 30 m^{-1}$, these irregular objects merge and gradually coalesce into morphologically stable, nearly spherical oscillons at $\sim 100 m^{-1}$, with an average physical size of approximately $1 \sim 3 m^{-1}$. At later times, the oscillon size exhibits further growth, which depends on h : smaller h leads to more pronounced growth. For $h = 0$ the growth of oscillons persists for a much longer duration, indicating an exceptionally long lifetime. In contrast, for $h \neq 0$ the

¹ In our simulation tests with $N = 512$, we find the lifetime in these models is longer than $3000 m^{-1}$. This implies that a significantly larger lattice grid number is required to accurately capture their full lifetime.

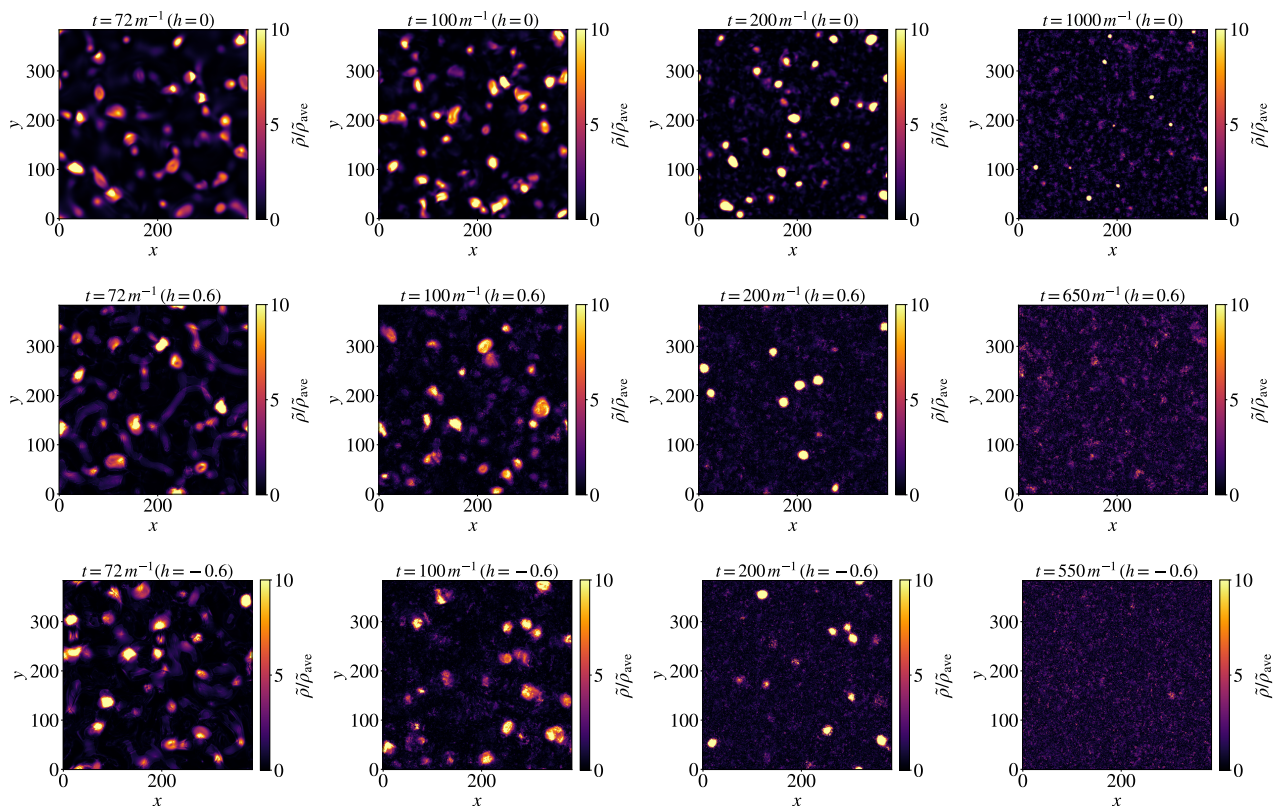


FIG. 7. Two-dimensional snapshots of overdense objects for $h = 0$ and $h = \pm 0.6$. The snapshots correspond to slices at $z = 0$ of the simulation grid. The leftmost column corresponds to times close to the end of the resonance stage.

growth duration is significantly shorter and the maximal size is reduced, remaining below $\sim 4 m^{-1}$; for example, for $h = 0.6$ the oscillon size is nearly constant before decay. For $h \gtrsim 0.2$, we observe a sharp decrease in the oscillon size within the simulated time window, signaling the decay of oscillons. After decay, the remnants become small size of density fluctuations with volumes below the minimal lattice cell; due to the finite resolution of our simulations, their final size in the figures does not vanish.

4. Energy and lifetime

Perhaps the most important properties of oscillons are their energy and lifetime. The total energy fraction of the overdense objects and the averaged energy contained per object are shown in figure 9. Only part of the oscillon energy is inherited from the resonance stage. At the end of resonance, dense objects contain 16% of the total energy for $\tilde{\rho}_{\text{th}} = 10 m$ ($\sim 38\%$ for $\tilde{\rho}_{\text{th}} = 5 m$), with negligible dependence on h . Consistent with our earlier discussion on the gradient energy, we find that the potential feature has negligible influence on energy transfer in the resonance regime.

Since oscillons are relatively stable and approximately spherically symmetric objects, we examine the energy

fraction in dense regions and the average energy per object. Combined with the earlier analysis of their morphology, we identify that oscillons form at $t \sim 100 m^{-1}$, after which the oscillon energy begins to grow steadily and their morphology becomes essentially stable. In the interval between the end of resonance and oscillon formation, the energy of dense regions continues to increase due to the self-interaction of the potential. The magnitude of this energy growth depends on h , with smaller h leading to a larger increase. Consequently, the $h = 0$ case exhibits the largest growth, reaching a final energy fraction of $\sim 45\%$, whereas for $h = 0.6$ the fraction peaks at only $\sim 32\%$. Larger values of h correspond to a shorter growth phase and an earlier onset of decay. Examining individual oscillons, we find that for $h \neq 0$ the average energy contained per oscillon is significantly lower than in the $h = 0$ case. This is consistent with our earlier analysis of oscillon sizes, since larger oscillons typically carry more energy.

Now let us study the lifetime of oscillons. The present work will focus on a statistical analysis of their collective characteristics. It was suggested that the oscillon lifetime could be determined from the time at which the gradient energy in the simulation box decays as a^{-3} [37]. However, we argue that this method is not sufficiently accurate. The gradient energy is distributed throughout the simulation volume, with oscillons accounting for only

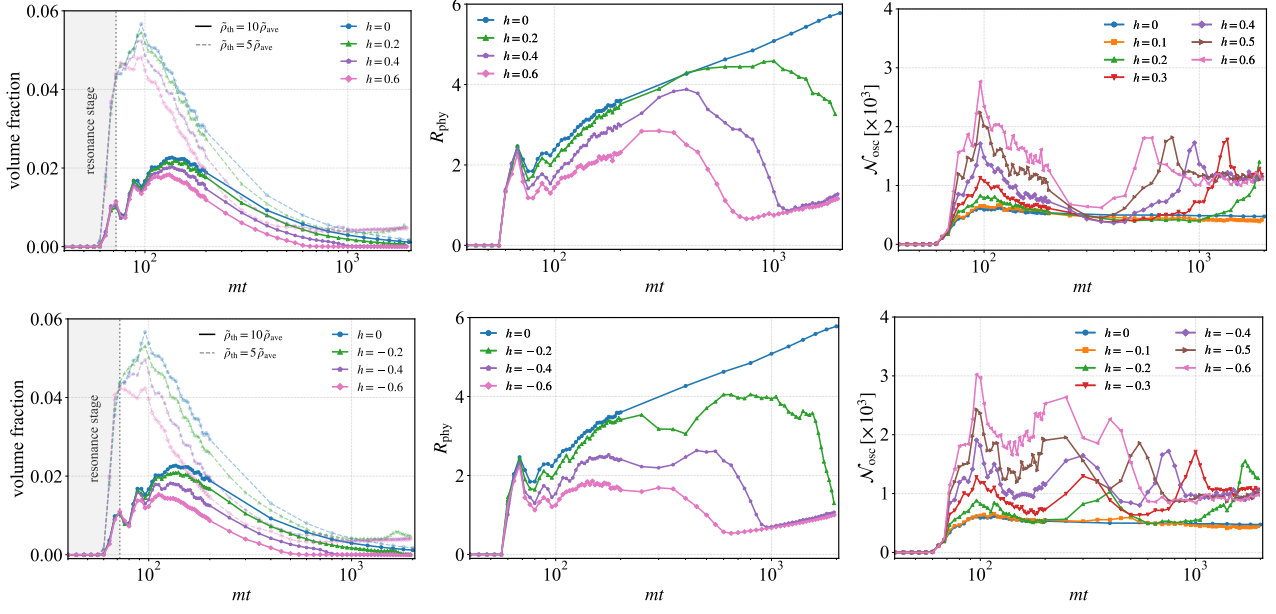


FIG. 8. The volume fraction (left), averaged physical size (middle), and number (right) of the dense objects for P_1 (upper) and P_2 (lower) set of parameters. The volume fraction of high density regions are shown for both threshold energy densities $5\tilde{\rho}_{\text{ave}}$ (light dashed) and $10\tilde{\rho}_{\text{ave}}$ (dark solid).

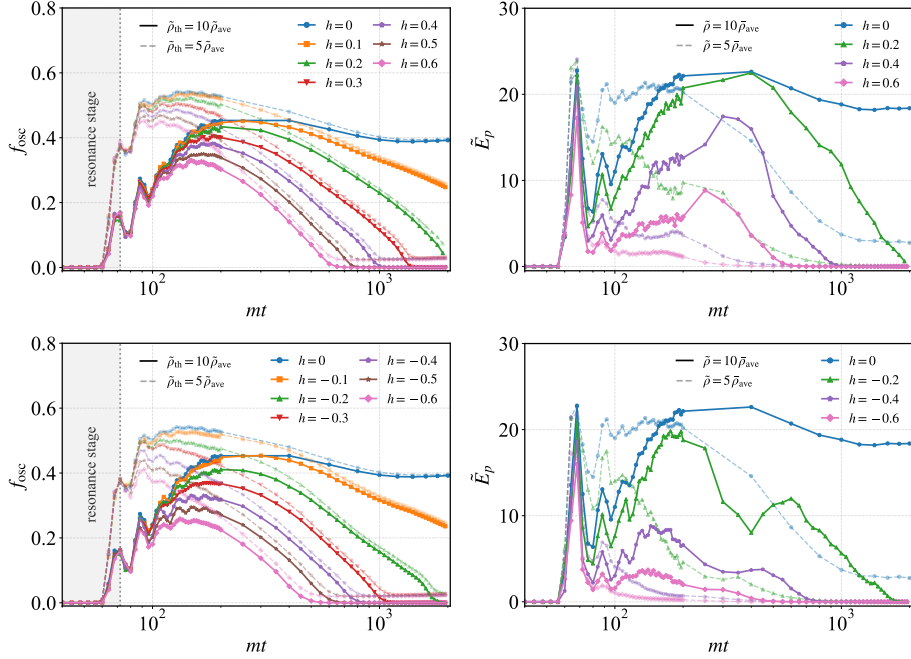


FIG. 9. The energy fraction of the dense objects (left) and the energy contained per object (right) for P_1 (upper) and P_2 (lower) set of parameters. In the left panel, we show the energy fraction for threshold energy densities set to five (light dashed) and ten (dark solid) times the mean density.

a fraction of it. Because the evolution of gradient energy inside and outside of the oscillons differs, tracking the total gradient energy cannot reliably determine the oscillon lifetime.

To see this more clearly, let us track the evolution

of the gradient energy inside and outside of the oscillons. We extract the gradient energy inside and outside of the oscillons from the HDF5 data and the results are shown in figures 10. Clearly, for $h = 0$ the gradient energy contained inside the oscillons exceeds that of out-

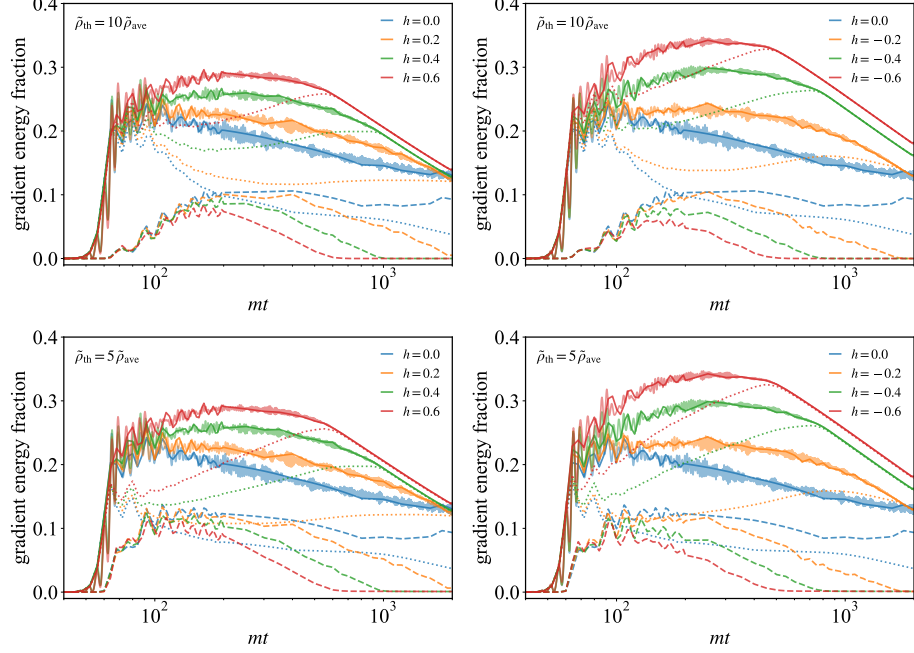


FIG. 10. The gradient energy distribution. The dashed and dotted curves denote the fractions of gradient energy inside and outside oscillons, respectively, whose sum gives the total gradient energy. The light solid curves correspond to the gradient energy from the `txt` outputs of *CosmoLattice*, while the dark solid curves show the gradient energy extracted from the `HDF5` data. The upper (lower) row adopts a threshold of 10 (5) times the average energy density.

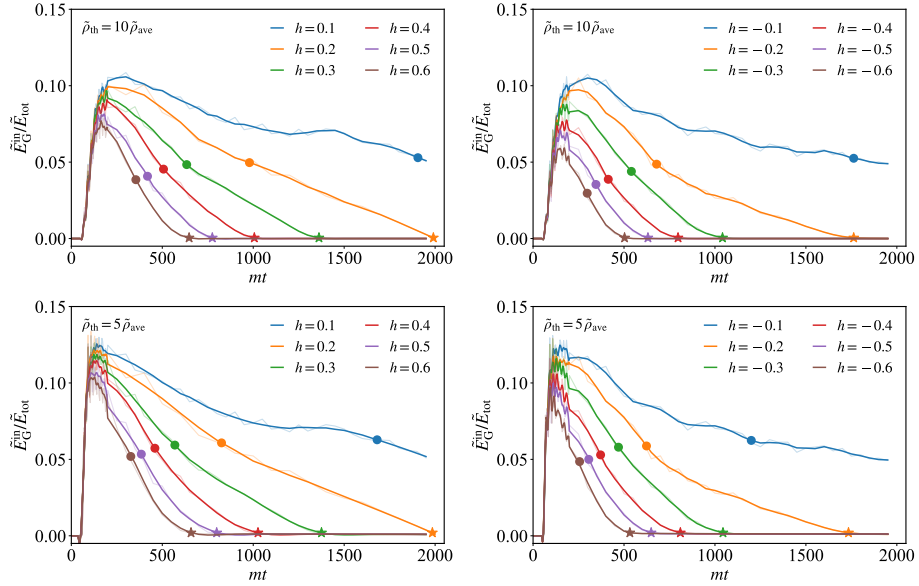


FIG. 11. The oscillon lifetime estimated by the decay of gradient energy. The light solid curves show the gradient energy fraction inside the oscillons extracted from the `HDF5` data files, while the dark solid curves correspond to the oscillation-averaged and smoothed results. Circle markers indicate the time at which the oscillons' gradient energy decays to 50% of its peak value, and star markers denote the time when the gradient energy decays to approximately zero.

side, whereas for $h \neq 0$ the gradient energy is predominantly distributed outside the oscillons. More importantly, we find that the evolution of the gradient energy inside and outside of the oscillons is qualitatively different. For $h = 0$, the fraction of gradient energy contained inside of the oscillons remains approximately constant, indicating that this component redshifts as a^{-3} , characteristic of matter-like behavior. In contrast, the gradient energy fraction outside oscillons decreases with time, implying that the total gradient energy does not scale globally as a^{-3} . For $h \neq 0$, the gradient energy fraction inside oscillons decays approximately linearly with time, with the decay rate increasing for larger values of h ; the gradient energy outside oscillons exhibits a more intricate behavior: for larger values of h , the external component undergoes a period of growth, partially sourced by the energy released during oscillon decay. Once the energy inside oscillons has decayed to zero, i.e., after the complete decay of oscillons, the total gradient energy fraction in the box exhibits a power-law decay in time, appearing as a straight line on a logarithmic vertical scale in figures. Consequently, in all cases we find that the total gradient energy within the simulation box does not redshift as a^{-3} . These observations indicate that the total gradient energy may not provide a fully reliable measure of the oscillon lifetime and merits further examination. By contrast, the gradient energy evolution within the overdense objects provides a more robust diagnostic. Since there is no unique definition for the lifetime of oscillons, particularly in statistical calculations. We compute the characteristic decay times for the gradient energy inside oscillons, measuring both the time of decaying to 50% of its peak value and the time for its full dissipation. These two reference criteria are adopted because the 50% decay marks the stage at which the oscillon energy ceases to be dominant, while 100% decay indicates that even the longest-lived oscillons in the box have disappeared. From a statistical perspective, the averaged oscillon lifetime is expected to lie between these two limits. The results are shown in figure 11.

We also determine the oscillon lifetime by tracking its total energy—a more direct approach than monitoring the gradient energy alone. Following the same procedure applied to the gradient energy, we determine the 50% decay and full-decay times of the oscillon’s total energy. The results are given in figure 12. These results allow us to draw the following conclusions:

- The two approaches we used agree well for most of parameters considered. These results validate the reliability of the method employed in this work. The discrepancy between the two estimation methods becomes more pronounced for small $|h|$ ($\lesssim 0.2$). A plausible explanation is that, in these models, oscillons are long-lived, and toward the end of the simulations their comoving size becomes comparable to the lattice cell, leading to increased numerical uncertainties between the two methods.

- A nonzero h significantly shortens the oscillon lifetime, particularly for $|h| > 0.1$. The dependence of the lifetime on h is highly nonlinear. Moreover, the dependence of the oscillon lifetime on the sign of h is asymmetric: for negative h , the lifetime decreases slightly faster than for positive h . Consequently, dip-type features in the potential reduce the oscillon lifetime more efficiently than bump-type features.
- Oscillons identified using different threshold criteria ($10\times$ and $5\times\tilde{\rho}_{\text{ave}}$) exhibit comparable lifetimes, with only minor differences. This implies that, at late times most of the energy in high-density regions is carried by oscillons with energy density larger than $10\tilde{\rho}_{\text{ave}}$, with only negligible contribution from subdominant objects with energy density $5 \sim 10\tilde{\rho}_{\text{ave}}$.

Shorter oscillon lifetime implies that, in the presence of external couplings, the reheating process is likely to proceed more rapidly, thereby shortening its duration. This, in turn, could modify the expansion history of the universe and affect inflationary observable.

D. Equation of state

It is well known that during preheating, if the inflaton oscillates about the minimum of a potential of the form $V(\phi) \sim \phi^n$, the EoS is $\omega \sim (n-2)/(n+2)$ under the homogeneous field approximation [34, 130, 131]. However, once the anisotropic type of gradient energy contributions are taken into account, the EoS would deviate from this estimate. In our models, the copious formation of oscillons contains a significant fraction of gradient energy component, which can appreciably alter the cosmic energy budget and the EoS parameter, potentially modifying the expansion history.

Now let us study the evolution of the EoS during this process. Using equations (24) and (25), the EoS parameter can be obtained,

$$\langle\omega\rangle = \frac{\tilde{\rho}}{\tilde{p}} = \frac{\tilde{E}_K - \frac{1}{3}\tilde{E}_G - \tilde{V}}{\tilde{E}_K + \tilde{E}_G + \tilde{V}}. \quad (33)$$

We show the simulation results of the EoS and the corresponding scale factors in figure 13. In all models, the EoS parameter remains below 1/3, yet exhibits different evolutionary behaviors. At early times, the EoS is positive for all models and increases with the magnitude of h . These behaviors can be understood by analyzing the relative contributions of the various energy components for different values of h . Since the kinetic energy constitutes the dominant fraction (exceeding 45%), followed by the potential and gradient contributions, the pressure is primarily controlled by the kinetic component. Although a larger h enhances the gradient energy, it simultaneously increases the kinetic energy while reducing the potential

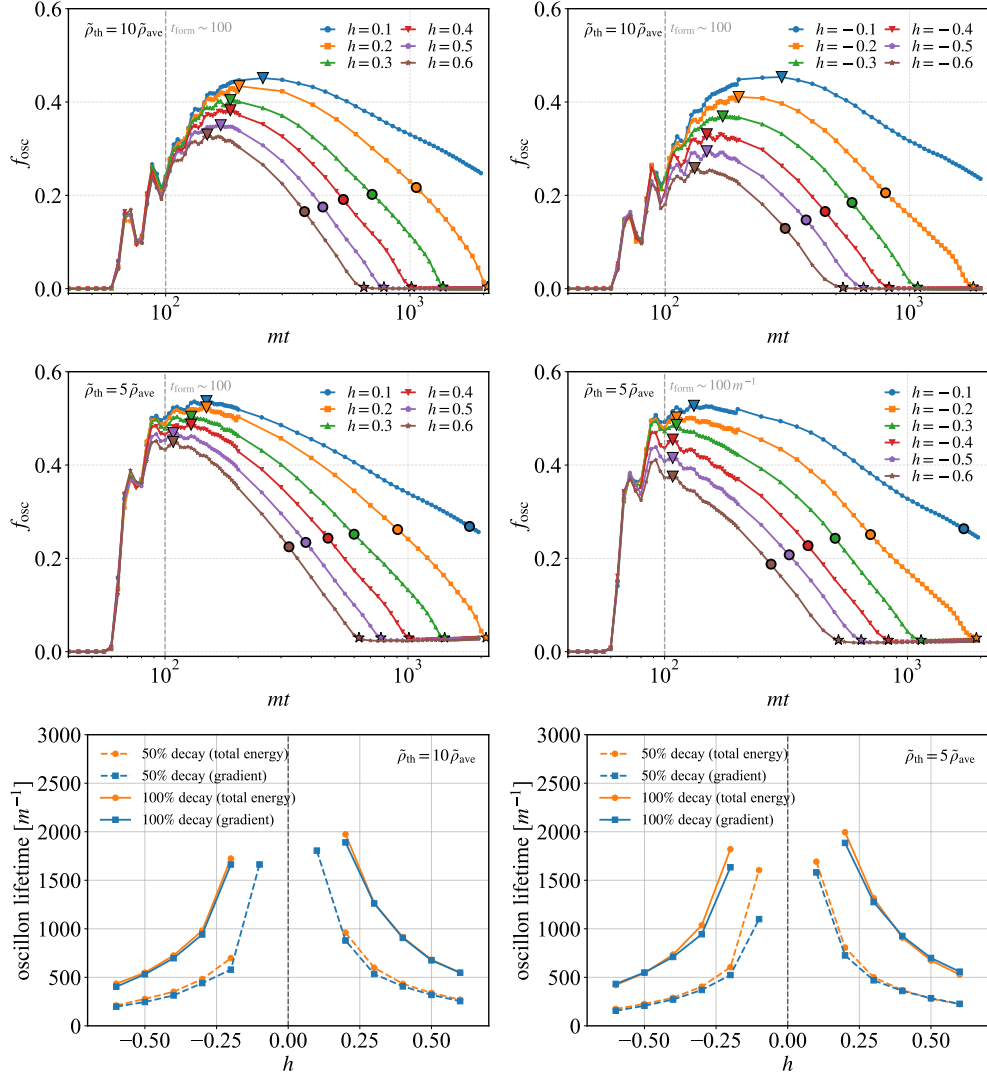


FIG. 12. Upper two rows: The oscillon lifetime estimated by the decay of the energy fraction of oscillons. Triangles mark the peak energy fraction attained by oscillons after formation, circles indicate the time when the energy fraction has decayed to 50% of its peak value, and stars denote the stage at which the energy has fully decayed. Third row: The dependence of the oscillon lifetime on the feature size parameter h .

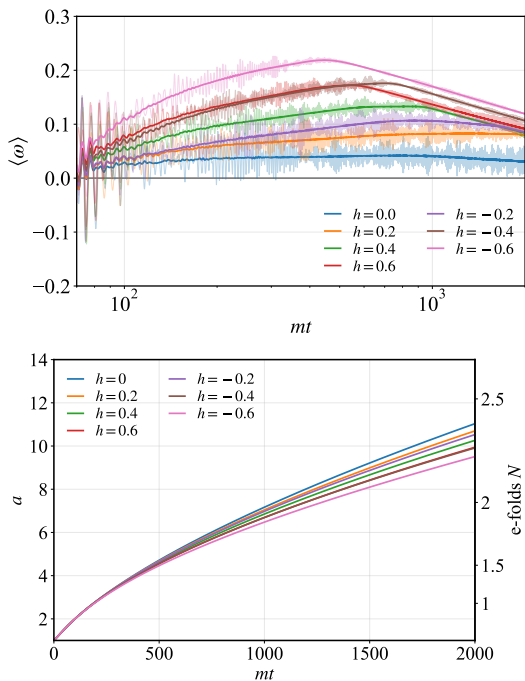


FIG. 13. The evolution of the EoS (left) and the scale factors (right).

energy. The net effect is an increase in the pressure \tilde{p} with h , accounting for the observed EoS behavior. Within the simulated time interval, the EoS parameter does not yet approach zero. Nevertheless, in the absence of external couplings, one expects that after the subsequent dissipation of gradient energy, the EoS will asymptotically approach zero, in agreement with the prediction of the homogeneous-field approximation.

In summary, larger $|h|$ results in a larger averaged EoS during preheating, thereby reducing the cosmic expansion rate. Short-lived oscillons imply that energy remains trapped in localized clump-like structures for shorter duration, thereby accelerating the transition of the Universe to a radiation-dominated era. These effects substantially influence the observable of the inflationary process [34, 43, 45, 132]. Quantifying them, however, requires a complete reheating process that accounts for inflaton couplings to external field(s), its full decay, and thermalization leading to radiation domination—aspects beyond the scope of this work. A quantitative assessment of these effects requires more detailed calculations; the more detailed investigation is left for future work.

E. Gravitational waves

It is well known that the anisotropic energy emerging during preheating would source a stochastic background of gravitational waves. To investigate the mechanism and dynamical properties of the gravitational wave production, we begin by introducing the tensor perturbations of

the metric that characterize gravitational waves:

$$ds^2 = -dt^2 + a^2(t)(\delta_{ij} + h_{ij})dx^i dx^j. \quad (34)$$

The equation of motion for the tensor perturbations h_{ij} is

$$\ddot{h}_{ij} + 3H\dot{h}_{ij} - \frac{\nabla^2}{a^2}h_{ij} = \frac{2}{M_P^2 a^2}\Pi_{ij}^{TT}, \quad (35)$$

where Π_{ij}^{TT} represents the transverse-traceless part of the effective anisotropic stress tensor $\Pi_{ij} = \partial_i\phi\partial_j\phi$. The energy density of the produced stochastic gravitational waves is

$$\begin{aligned} \rho_{\text{GW}}(t) &= \frac{M_P^2}{4}\langle\dot{h}_{ij}(\mathbf{x},t)\dot{h}_{ij}(\mathbf{x},t)\rangle \\ &\approx \frac{M_P^2}{4V}\int_V\frac{d^3\mathbf{k}}{(2\pi)^3}\dot{h}_{ij}(\mathbf{k},t)\dot{h}_{ij}^*(\mathbf{k},t) = \int\frac{d\rho_{\text{GW}}}{d\log k}d\log k, \end{aligned} \quad (36)$$

where the symbol $\langle\dots\rangle$ represents a spatial or temporal average. Since our simulation is performed within a box with finite volume, we adopt the spatial average throughout. The normalized gravitational wave energy density power spectrum (per logarithmic momentum interval) is then given by

$$\Omega(k,t) = \frac{1}{\rho_c}\frac{d\rho_{\text{GW}}}{d\log k}, \quad (37)$$

where ρ_c is the critical energy density.

We present in figure 14 representative results of the spectrum at production and at present day, including the standard T-model and the model with bump/dip. For the standard T-model, we find that the gravitational wave emission concentrates in the low-momentum modes and are mainly produced during the linear stage of parametric resonance, while the high-momentum modes are largely suppressed. For the parameters considered in this paper, gravitational waves are most strongly amplified in modes with momenta $k \lesssim 2m$. This behavior can be correlated with the power spectrum of the scalar field. For models with $h \neq 0$, gravitational waves in high-momentum modes are also excited significantly, but they are weaker than those in the low-momentum modes. This behavior may be attributed to the decay of short-lived oscillons, but this requires further confirmation. This constitutes the main difference with the gravitational wave spectra of the standard T-model, in which the high-momentum modes are rather weak.

Because of cosmic expansion, the energy density of the gravitational waves—which behave as radiation—is diluted, and their frequencies are redshifted. The energy density power spectrum and the redshifted frequency at present day are [133]

$$\begin{aligned} h^2\Omega_{\text{GW}}^{(0)}(f) &= h^2\Omega_{\text{rad},0}\left(\frac{a_e}{a_*}\right)^{1-3\omega_{\text{eff}}}\left(\frac{g_*}{g_0}\right)^{-1/3}\Omega_{\text{GW}}^{(e)}(k), \\ f &= 4 \times 10^{10}\left(\frac{a_e}{a_*}\right)^{\frac{1-3\omega_{\text{eff}}}{4}}\frac{k}{a_e\rho_e^{1/4}}\text{Hz}, \end{aligned} \quad (38)$$

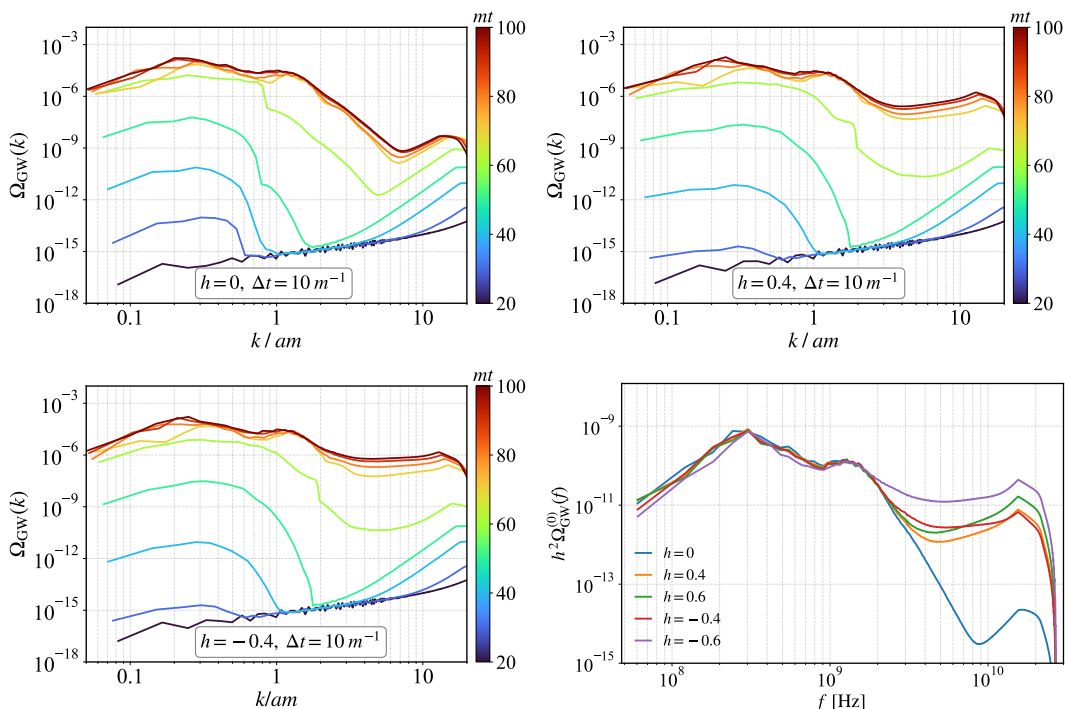


FIG. 14. The GW spectrum at production and at present day for selected models. To obtain the present-day gravitational wave spectrum, we identify the emission time t_e as the moment when the spectrum saturates and ceases to grow; this time is model dependent. For simplicity, we further assume that the effective EoS parameter remains $\omega_{\text{eff}} = 1/3$, which is equivalent to assuming that the universe enters a radiation dominated era immediately after gravitational wave production.

where $h^2 \Omega_{\text{rad},0} = 4.3 \times 10^{-5}$ is the abundance of radiation today and the subscripts “e”, “*”, and “0” denote the time of gravitational wave emission, the end of reheating, and present day, respectively. The emission time is chosen to be the time when the gravitational-wave spectrum becomes stationary, leading to a model-dependent choice of t_e . We set the ratio of the relativistic degrees of freedom at t_* and t_0 to $g_*/g_0 = 100$. The results are shown in lower right of figure 14. Note that, the reheating process has not yet been completed at gravitational wave emission time t_e . Subsequent inflaton decay and thermalization are still required for the universe to reach thermal equilibrium and enter the radiation dominated era. For simplicity, we adopt a rough approximation in which the universe is assumed to become radiation dominated immediately after t_e , corresponding to an effective EoS $\omega_{\text{eff}} = 1/3$ and hence $(a_e/a_*)^{1-3\omega_{\text{eff}}} = 1$. Taking into account the full reheating dynamics would introduce an additional suppression factor, reducing the resulting gravitational wave spectrum by a factor of a few. It is evident that these gravitational waves lie far beyond the sensitivity of current detectors [134–137]. However, one may constrain the gravitational waves indirectly, such as using the cosmological constraints on the effective number of relativistic degrees of freedom, see references [119, 138–141].

V. CONCLUSION AND DISCUSSION

Reheating serves as the transitional stage connecting inflation to the radiation dominated era, during which the energy stored in the inflaton field must be transferred to produce Standard Model particles through specific mechanisms. Due to the lack of direct observational probes, the detailed microphysics of reheating remains unclear, despite the existence of several well-motivated scenarios, such as parametric resonance.

In this exploratory work, we investigated a preheating model realized by an inflationary potential with characteristic structures, focusing on how such features modify the reheating dynamics, with linear and non-linear approaches. In linear approach, we mainly analyzed the resonance efficiency with Floquet analysis. We showed that the Floquet instability bands are deformed compared to the standard α -attractor T-model. This modifies the field range and also the perturbation modes in resonance. We then studied the self-resonance by performing nonlinear lattice simulation. The linear, nonlinear, and backreaction stages of the resonance are clearly identified by tracking the evolution of the fields and fluctuations. The existence of characteristic structures in the potential function slightly alters the evolution of the fluctuation (defined by the variance of the field in lattice). During self-resonance, a substantial fraction of the inflaton’s energy is transferred into its own fluctuations,

which are amplified to the nonlinear regime and give rise to spatially localized structures. We found that during the resonance stage the amount of gradient energy transferred from the homogeneous inflaton mode is nearly independent of h . After the resonance terminates, however, the subsequent evolution of the gradient energy exhibits a strong dependence on h : for small h it gradually decays, whereas for larger magnitude of h it undergoes a pronounced growth. Thus, while the presence of h does not affect energy transfer during resonance, it significantly modifies the energy conversion in the subsequent stage.

We further investigated the formation and properties of oscillons statistically. Compared to the $h = 0$ model, models with nonzero h lead to the production of a larger number of oscillons that are smaller in size. In all models with $h \neq 0$, the energy fraction stored in oscillons is smaller than in the $h = 0$ case, and this suppression becomes increasingly pronounced with growing $|h|$. By comparing the evolution of the total gradient energy with that inside and outside oscillons, we demonstrated that the oscillon lifetime cannot be determined from the total gradient energy alone. Instead, to quantify the oscillon lifetime, we track both the gradient energy and the total energy confined within the high density regions identified as oscillons. This distinction is essential because, in models with $h \neq 0$, a substantial amount of gradient energy resides in low density regions outside the oscillons, which would otherwise contaminate the lifetime estimation. We found that oscillons in all $h \neq 0$ models have systematically shorter lifetimes, with the effect strengthening as $|h|$ increases. For larger values of h ($\gtrsim 0.2$), the evolution over the entire oscillon lifetime can be resolved with good accuracy, whereas for smaller h (< 0.2) we estimate that larger lattice grid number ($N > 512$) is required to reliably track the evolution. Although the numerical values of oscillon lifetimes depend on the specific definitions of lifetime and the threshold criteria, we found that their dependence on the parameter h exhibits a similar trend across different thresholds, despite the limited size of our sample. These spatially localized structures have important implications for the cosmic expansion history: they modify the energy distribution and the expansion history of the universe, thereby affecting inflationary observable. Although a full reheating simulation is required for a quantitative characterization of these effects, noticeable differences are already evident within the time span of our simulations.

We also examined the production of gravitational waves. We found that the gravitational waves are generated predominantly during the resonance stage, while their production becomes strongly suppressed once oscillons form and settle into a quasi-stable configuration, in agreement with previous studies. The presence of characteristic features in the potential leaves the low-frequency part of the gravitational-wave spectrum essentially unchanged, but significantly modifies the high-frequency energy spectrum. Although these features are currently beyond direct detectability, they may be indirectly con-

strained by future high-precision cosmological observations.

This work focus on the self-resonance mechanism in the absence of external couplings and therefore do not provide a complete description of the reheating process. A comprehensive investigation of the impact of potential features on the cosmic evolution history and observable requires the inclusion of external couplings, as well as the subsequent decay and thermalization toward equilibrium. Besides, the calculation of the gravitational-wave spectrum depends sensitively on the detailed reheating history, including the duration between gravitational-wave emission and the end of reheating and the effective EoS parameter during this period. A complete treatment of reheating is thus essential for a quantitative understanding of the cosmological effects induced by potential features. We leave these issues for future work. The nonlinear study of reheating places stringent demands on the accuracy of lattice simulations. Owing to computational limitations, our simulations are performed on lattice with 384^3 grids. Higher-resolution and longer time of simulations will be crucial for a more precise characterization of the reheating dynamics and may reveal additional phenomena. In particular, recent works [58, 61, 63], however, have suggested that oscillons may undergo gravitational collapse and form PBHs. In such scenarios, the FRW background approximation breaks down and gravitational collapse effects must be taken into account. Future studies employing higher-resolution computations and combining lattice simulations with numerical relativity will therefore be essential for exploring reheating with potential features and may uncover further novel phenomena.

VI. ACKNOWLEDGMENTS

We are grateful to the High-Performance Computing Platform of the Basic Physics Experiment Center at Nanchang University for supporting part of the lattice simulations. We thank Shao-Wen Wei, Ke Yang, Wen-Di Guo, and Peng Cheng for valuable discussions. B.-M. Gu thanks Lanzhou Center for Theoretical Physics for its hospitality during his visit, where this work was originally initiated. This work is partially supported by the National Natural Science Foundation of China (Grants No. 12165013, 12375049, 12575055, 12247101, 12475056, and 12247101). Y.-P. Zhang is supported by ‘‘Talent Scientific Fund of Lanzhou University’’. F.-W. Shu is supported by the Key Program of the Natural Science Foundation of Jiangxi Province under Grant No. 20232ACB201008, and the Ganpo High-Level Innovative Talent Program.

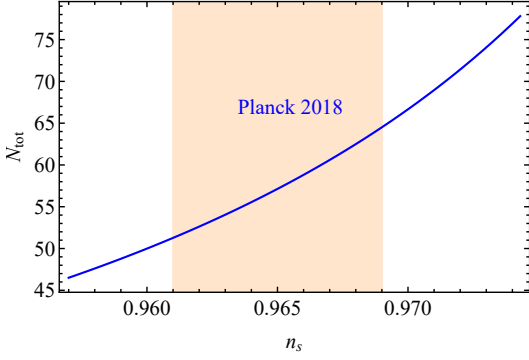


FIG. 15. The plot of N_{tot} versus n_s for $\alpha = 10^{-4}M_P^2$ ($\lambda = 50\sqrt{\frac{2}{3}}$). The dashed regions are the constraints from Planck 2018.

Appendix A: Model parameters of T-model

The model parameters can be constrained by the CMB constraints on the spectral index n_s and the amplitude of the scalar power spectrum A_s . For $n = 1$ of (12), it is straightforward to obtain

$$n_s = 1 - 6\epsilon_V + 2\eta_V = 1 - 8\lambda^2 \text{csch}^2\left(\lambda \frac{\phi}{M_P}\right). \quad (\text{A1})$$

Thus the field value at horizon crossing is

$$\phi_* = \frac{1}{\lambda} \text{arcsinh}\left(2\lambda \sqrt{\frac{2}{1-n_s}}\right). \quad (\text{A2})$$

The amplitude of the power spectrum at horizon crossing is

$$A_s = \frac{H^2(\phi_*)}{8\pi^2\epsilon_V(\phi_*)} = \frac{4\lambda^2 V_0}{3\pi^2(1-n_s)^2} = 2.1 \times 10^{-9}. \quad (\text{A3})$$

For a given λ , the observational constraints on n_s and A_s limits V_0 . The field value at the end of inflation is defined by $\epsilon_V(\phi_{\text{end}}) = 1$, which gives

$$\phi_{\text{end}} = \frac{1}{2\lambda} \text{arcsinh}\left(2\sqrt{2}\lambda\right). \quad (\text{A4})$$

Using equations (A2) and (A4) we immediately get the total e-folds of inflation

$$N_{\text{tot}} = \int_{\phi_{\text{end}}}^{\phi_*} \frac{d\phi}{\sqrt{2\epsilon_V}} = \frac{2}{1-n_s} - \frac{\sqrt{1+8\lambda^2}-1}{8\lambda^2}. \quad (\text{A5})$$

We show the plot of e -folds in figure 15. In this work we set $\alpha = 10^{-4}M_P^2$ (corresponds to $\lambda = 50\sqrt{\frac{2}{3}}$) and $V_0 = 1.14 \times 10^{-14}M_P^4$, yielding $n_s = 0.965$ and $N_{\text{tot}} \simeq 57$.

Appendix B: Derivation of the Floquet exponent

We compute the Floquet exponent following the procedure outlined in [25]. We first recast equation (14) into

a first-order formalism,

$$\dot{x}(t) = U(t)x(t), \quad U(t) = \begin{pmatrix} 0 & 1 \\ -k^2 - V''(\phi(t)) & 0 \end{pmatrix}, \quad (\text{B1})$$

where $x(t) = [\delta\phi_k, \delta\pi_k]^T$ with $\delta\pi_k = \delta\dot{\phi}_k$. Next, we need to calculate the time period T of $U(t)$. The period is defined by

$$T = 2 \int_{\phi_{\text{min}}}^{\phi_{\text{max}}} \frac{d\phi}{\sqrt{2V(\phi_{\text{max}}) - 2V(\phi)}}, \quad (\text{B2})$$

where $\phi_{\text{max}} = \phi_i$ and ϕ_{min} is obtained by solving $V(\phi_{\text{min}}) = V(\phi_{\text{max}})$. Then, we solve the static version ($H = 0$ and $a = 1$) of the scalar field equation (3) and the perturbed equation (14) with two sets of initial conditions $\{\delta\phi_k^{(1)}(0) = 1, \delta\pi_k^{(1)}(0) = 0\}$ and $\{\delta\phi_k^{(2)}(0) = 0, \delta\pi_k^{(2)}(0) = 1\}$, from 0 to T . At last, the Floquet exponent can be obtained by

$$\Re\epsilon[\mu_k^\pm] = \frac{1}{T} |\ln o_k^\pm|, \quad (\text{B3})$$

where

$$o_k^\pm = \frac{\delta\phi_k^{(1)} + \delta\pi_k^{(2)}}{2} \pm \frac{\sqrt{(\delta\phi_k^{(1)} - \delta\pi_k^{(2)})^2 + 4\delta\phi_k^{(2)}\delta\pi_k^{(1)}}}{2}, \quad (\text{B4})$$

with all quantities evaluated at $t = T$. Since (16) contains both of the growing and decaying branches of solution, it exhibits exponential growth whenever $\Re\epsilon[\mu_k] \neq 0$. For convenience, we therefore restrict ourselves to the case $\Re\epsilon[\mu_k] > 0$.

Appendix C: Convergence test

It is important to emphasize that the simulation is performed in comoving coordinates, so that the simulation volume remains fixed throughout the evolution. As the universe expands, objects with fixed physical size therefore appear progressively smaller in the box. Consequently, although oscillons are initially well resolved with characteristic scales much larger than the lattice spacing, their comoving size eventually becomes comparable to a single lattice cell. At this point, the lattice simulation can no longer capture oscillon dynamics, marking the breakdown of the lattice simulation. Assuming the physical size of an oscillon is L_{osc} (typically of order several m^{-1}), the breakdown of the simulation occurs when the lattice spacing becomes comparable to the comoving size of the oscillon

$$dx \equiv \frac{2\pi}{N k_{\text{IR}}} \simeq \frac{L_{\text{osc}}}{a(t_{\text{br}})}, \quad (\text{C1})$$

where dx is the lattice spacing in comoving coordinate. Consequently, the simulations are trustable only for

$$a \lesssim \frac{N}{2\pi} k_{\text{IR}} L_{\text{osc}}. \quad (\text{C2})$$

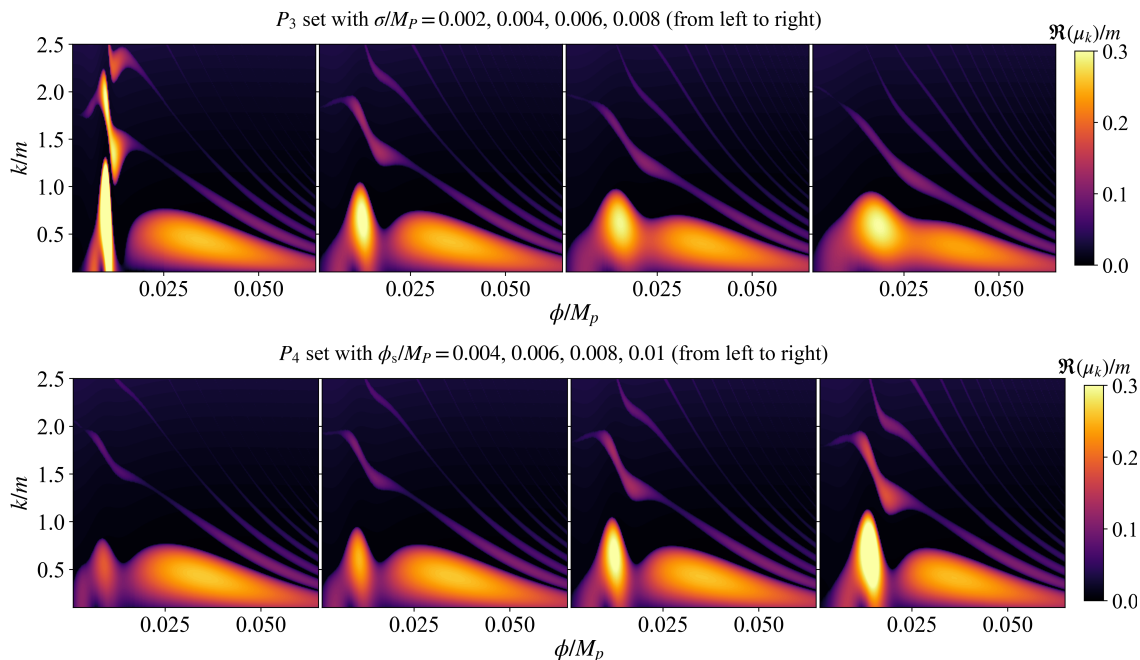


FIG. 16. The Floquet charts showing the instability bands of the deformed T-model for P_3 (upper) and P_4 (lower) parameters, with cosmic expansion neglected. Note that the Floquet exponent is scaled by the inflaton mass m and $H_i \simeq 0.01 m$ for $\alpha = 10^{-4} M_P^2$.

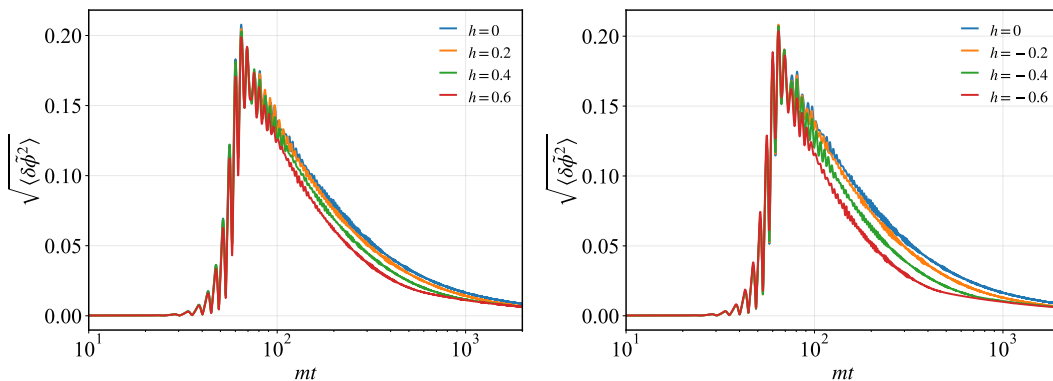


FIG. 17. Evolution of the fluctuations, corresponding to the parameter sets P_1 (left) and P_2 (right).

A careful choice of the lattice grid number N and the infrared cutoff k_{IR} is therefore essential for sufficient resolution. Larger N and higher cutoff wavenumbers generally extend the reliable simulation time. However, as can be seen from the Floquet charts in figure 3, the resonant modes are mainly confined to $k < m$, k_{IR} cannot be too large, as excluding these modes would degrade the description of the preheating dynamics. Hence, in practice, obtaining more reliable simulations over longer time scales generally requires increasing the lattice grid number N .

To assess the robustness of our numerical results, we performed convergence tests with $k_{\text{IR}} = 0.1 m$ and using grid points of $N^3 = 128^3$, 256^3 , 384^3 , and 512^3 . As an illustration, we compare the gradient energy computed

at different lattice resolutions, with the results shown in figure 18. We expect that increasing the grid number N leads to more accurate results. As shown, the lattice with $N^3 = 128^3$ grids are insufficient to faithfully capture the formation and subsequent evolution of oscillons; at this resolution, the evolution of the gradient energy is only qualitatively captured up to $t \sim 300 m^{-1}$, beyond which the numerical errors become very large. For $N^3 = 256^3$, the simulation remains reliable up to $t_{\text{br}} \simeq 1000 m^{-1}$ ($a_{\text{br}} \simeq 7.1$). Based on this result, we obtain a conservative estimate for the characteristic oscillon scale, $L_{\text{osc}} \sim 1.75 m^{-1}$. Using this characteristic oscillon scale, we predict that the simulation breaks down at $t_{\text{br}} \simeq 1900 m^{-1}$ ($a_{\text{br}} \simeq 10.7$) for $N^3 = 384^3$, while for $N^3 = 512^3$ the corresponding breakdown occurs at

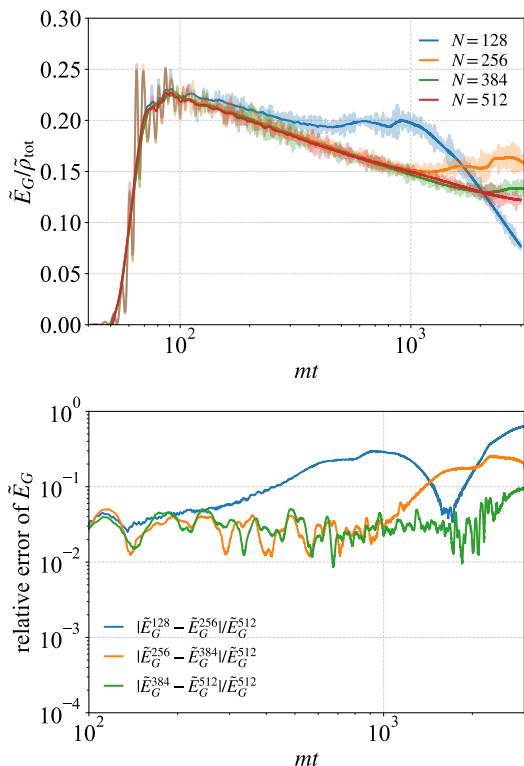


FIG. 18. The gradient energy fraction for the T-model ($h = 0$) with different resolutions (left) and the relative errors (right). We find that, for k_{IR} , simulations with $N = 256$ remain reliable up to $t \lesssim 1000 m^{-1}$, while increasing the resolution to $N = 384$ extends the trustworthy regime to approximately $t \sim 2000 m^{-1}$, in both cases, the relative errors remain below $\sim 3\%$ within these intervals.

$t_{\text{br}} \simeq 2900 m^{-1}$ ($a_{\text{br}} \simeq 14.3$). These estimates are consistent with the convergence tests presented in figure 18. As shown in the figure, the results for $N^3 = 384^3$ are reliable for $t \lesssim 2000 m^{-1}$, whereas for $N = 512$ the reliable regime extends to $\sim 3000 m^{-1}$. Since, in most cases of our model, the oscillon lifetime is shorter than $2000 m^{-1}$, we therefore adopt $N^3 = 384^3$ as a compromise that ensures sufficient accuracy while significantly reducing the computational cost.

Appendix D: The role of parameters σ (width) and ϕ_s (location)

We consider the parameter sets listed in table II, which corresponds to different widths and locations of potential feature. The Floquet charts are shown in figure (16). The parameter σ determines the width of the new resonance band. Generally, A sharp feature in the potential narrows the field range of the emerging resonance band while markedly enhancing its Floquet exponent. At the same time, it extends the coverage in momentum space, allowing a broader set of fluctuation modes to resonate.

For example, when $\sigma = 0.002 M_P$, nearly all modes in $0 < k < 2.5m$ undergo resonance around the potential feature. The results of different location parameter shows that, for a fixed h , the farther the potential feature is from the minimum (larger ϕ_s), the greater the deviation from the original T-model, resulting in a stronger newly generated resonance.

Sets	$V_0 [M_p^4]$	$\alpha [M_p^2]$	h	$\sigma [M_p]$	$\phi_s [M_p]$
P_3	1.14×10^{-14}	10^{-4}	0.6	2×10^{-3}	8×10^{-3}
				4×10^{-3}	8×10^{-3}
				6×10^{-3}	8×10^{-3}
				8×10^{-3}	8×10^{-3}
P_4	1.14×10^{-14}	10^{-4}	0.6	4×10^{-3}	4×10^{-3}
				4×10^{-3}	6×10^{-3}
				4×10^{-3}	8×10^{-3}
				4×10^{-3}	10×10^{-3}

TABLE II. The parameter sets P_3 and P_4 .

- [1] A. A. Starobinsky, *Phys. Lett. B* **91**, 99 (1980).
- [2] A. H. Guth, *Phys. Rev. D* **23**, 347 (1981).
- [3] A. D. Linde, *Phys. Lett. B* **108**, 389 (1982).
- [4] A. Albrecht and P. J. Steinhardt, *Phys. Rev. Lett.* **48**, 1220 (1982).
- [5] A. D. Linde, *Phys. Lett. B* **129**, 177 (1983).
- [6] N. Aghanim *et al.* (Planck), *Astron. Astrophys.* **641**, A6 (2020), [Erratum: *Astron. Astrophys.* 652, C4 (2021)], [arXiv:1807.06209 \[astro-ph.CO\]](#).
- [7] Y. Akrami *et al.* (Planck), *Astron. Astrophys.* **641**, A10 (2020), [arXiv:1807.06211 \[astro-ph.CO\]](#).
- [8] T. Louis *et al.* (Atacama Cosmology Telescope), *JCAP* **11**, 062, [arXiv:2503.14452 \[astro-ph.CO\]](#).
- [9] E. Calabrese *et al.* (Atacama Cosmology Telescope), *JCAP* **11**, 063, [arXiv:2503.14454 \[astro-ph.CO\]](#).
- [10] L. F. Abbott, E. Farhi, and M. B. Wise, *Phys. Lett. B* **117**, 29 (1982).
- [11] A. D. Dolgov and D. P. Kirilova, *Sov. J. Nucl. Phys.* **51**, 172 (1990).
- [12] J. H. Traschen and R. H. Brandenberger, *Phys. Rev. D* **42**, 2491 (1990).
- [13] D. Boyanovsky, H. J. de Vega, and R. Holman, *Phys. Rev. D* **49**, 2769 (1994), [arXiv:hep-ph/9310319](#).
- [14] D. Boyanovsky, H. J. de Vega, R. Holman, D. S. Lee, and A. Singh, *Phys. Rev. D* **51**, 4419 (1995), [arXiv:hep-ph/9408214](#).
- [15] L. Kofman, A. D. Linde, and A. A. Starobinsky, *Phys. Rev. Lett.* **73**, 3195 (1994), [arXiv:hep-th/9405187 \[hep-th\]](#).
- [16] Y. Shtanov, J. H. Traschen, and R. H. Brandenberger, *Phys. Rev. D* **51**, 5438 (1995), [arXiv:hep-ph/9407247 \[hep-ph\]](#).
- [17] L. Kofman, A. D. Linde, and A. A. Starobinsky, *Phys. Rev. D* **56**, 3258 (1997), [arXiv:hep-ph/9704452](#).
- [18] M. Gleiser, *Phys. Rev. D* **49**, 2978 (1994), [arXiv:hep-ph/9308279](#).
- [19] M. A. Amin, (2010), [arXiv:1006.3075 \[astro-ph.CO\]](#).
- [20] M. A. Amin, R. Easther, and H. Finkel, *JCAP* **12**, 001, [arXiv:1009.2505 \[astro-ph.CO\]](#).
- [21] M. A. Amin, R. Easther, H. Finkel, R. Flauger, and M. P. Hertzberg, *Phys. Rev. Lett.* **108**, 241302 (2012), [arXiv:1106.3335 \[astro-ph.CO\]](#).
- [22] B. A. Bassett, S. Tsujikawa, and D. Wands, *Rev. Mod. Phys.* **78**, 537 (2006), [arXiv:astro-ph/0507632 \[astro-ph\]](#).
- [23] R. Allahverdi, R. Brandenberger, F.-Y. Cyr-Racine, and A. Mazumdar, *Ann. Rev. Nucl. Part. Sci.* **60**, 27 (2010), [arXiv:1001.2600 \[hep-th\]](#).
- [24] K. D. Lozanov, (2019), [arXiv:1907.04402 \[astro-ph.CO\]](#).
- [25] M. A. Amin, M. P. Hertzberg, D. I. Kaiser, and J. Karouby, *Int. J. Mod. Phys. D* **24**, 1530003 (2014), [arXiv:1410.3808 \[hep-ph\]](#).
- [26] X.-X. Kou, C. Tian, and S.-Y. Zhou, *Class. Quant. Grav.* **38**, 045005 (2021), [arXiv:1912.09658 \[gr-qc\]](#).
- [27] J. C. Aurrekoetxea, K. Clough, and F. Muia, *Phys. Rev. D* **108**, 023501 (2023), [arXiv:2304.01673 \[gr-qc\]](#).
- [28] S.-Y. Zhou, E. J. Copeland, R. Easther, H. Finkel, Z.-G. Mou, and P. M. Saffin, *JHEP* **10**, 026, [arXiv:1304.6094 \[astro-ph.CO\]](#).
- [29] D. G. Levkov and V. E. Maslov, *Phys. Rev. D* **108**, 063514 (2023), [arXiv:2306.06171 \[hep-th\]](#).
- [30] T. Jia, Y. Sang, and X. Zhang, *Phys. Rev. D* **111**, 083531 (2025), [arXiv:2409.04046 \[astro-ph.CO\]](#).
- [31] J. Liu, Z.-K. Guo, R.-G. Cai, and G. Shiu, *Phys. Rev. Lett.* **120**, 031301 (2018), [arXiv:1707.09841 \[astro-ph.CO\]](#).
- [32] S. Antusch, F. Cefala, S. Krippendorff, F. Muia, S. Orani, and F. Quevedo, *JHEP* **01**, 083, [arXiv:1708.08922 \[hep-th\]](#).
- [33] S. Kasuya, M. Kawasaki, F. Otani, and E. Sonomoto, *Phys. Rev. D* **102**, 043016 (2020), [arXiv:2001.02582 \[hep-ph\]](#).
- [34] K. D. Lozanov and M. A. Amin, *Phys. Rev. D* **97**, 023533 (2018), [arXiv:1710.06851 \[astro-ph.CO\]](#).
- [35] H.-Y. Zhang, *JCAP* **03**, 102, [arXiv:2011.11720 \[hep-th\]](#).
- [36] R. Mahbub and S. S. Mishra, *Phys. Rev. D* **108**, 063524 (2023), [arXiv:2303.07503 \[astro-ph.CO\]](#).
- [37] M. Shafi, E. J. Copeland, R. Mahbub, S. S. Mishra, and S. Basak, *JCAP* **10**, 082, [arXiv:2406.00108 \[hep-ph\]](#).
- [38] S. Antusch and S. Orani, *JCAP* **03**, 026, [arXiv:1511.02336 \[hep-ph\]](#).
- [39] S. Antusch, F. Cefalà, and F. Torrentí, *JCAP* **10**, 002, [arXiv:1907.00611 \[hep-ph\]](#).
- [40] M. A. Amin, *Phys. Rev. D* **87**, 123505 (2013), [arXiv:1303.1102 \[astro-ph.CO\]](#).
- [41] Y. Sang and Q.-G. Huang, *Phys. Lett. B* **823**, 136781 (2021), [arXiv:2012.14697 \[hep-th\]](#).
- [42] K. D. Lozanov and M. A. Amin, *Phys. Rev. Lett.* **119**, 061301 (2017), [arXiv:1608.01213 \[astro-ph.CO\]](#).

- [43] S. Antusch, D. G. Figueroa, K. Marschall, and F. Torrenti, *Phys. Lett. B* **811**, 135888 (2020), [arXiv:2005.07563 \[astro-ph.CO\]](#).
- [44] A. K. Soman, S. S. Mishra, M. Shafi, and S. Basak, *Phys. Rev. D* **112**, 103521 (2025), [arXiv:2407.07956 \[gr-qc\]](#).
- [45] S. Antusch, K. Marschall, and F. Torrenti, *JCAP* **11**, 002, [arXiv:2507.13465 \[astro-ph.CO\]](#).
- [46] S. Antusch, F. Cefala, and S. Orani, *JCAP* **03**, 032, [arXiv:1712.03231 \[astro-ph.CO\]](#).
- [47] D. G. Figueroa and F. Torrenti, *JCAP* **10**, 057, [arXiv:1707.04533 \[astro-ph.CO\]](#).
- [48] J. Liu, Z.-K. Guo, R.-G. Cai, and G. Shiu, *Phys. Rev. D* **99**, 103506 (2019), [arXiv:1812.09235 \[astro-ph.CO\]](#).
- [49] M. A. Amin, J. Braden, E. J. Copeland, J. T. Giblin, C. Solorio, Z. J. Weiner, and S.-Y. Zhou, *Phys. Rev. D* **98**, 024040 (2018), [arXiv:1803.08047 \[astro-ph.CO\]](#).
- [50] K. D. Lozanov and M. A. Amin, *Phys. Rev. D* **99**, 123504 (2019), [arXiv:1902.06736 \[astro-ph.CO\]](#).
- [51] Y. Sang and Q.-G. Huang, *Phys. Rev. D* **100**, 063516 (2019), [arXiv:1905.00371 \[astro-ph.CO\]](#).
- [52] J. Li, H. Yu, and P. Wu, *Phys. Rev. D* **102**, 083522 (2020).
- [53] T. Hiramatsu, E. I. Sfakianakis, and M. Yamaguchi, *JHEP* **03**, 021, [arXiv:2011.12201 \[hep-ph\]](#).
- [54] X.-X. Kou, J. B. Mertens, C. Tian, and S.-Y. Zhou, *Phys. Rev. D* **105**, 123505 (2022), [arXiv:2112.07626 \[gr-qc\]](#).
- [55] T. Krajewski and K. Turzyński, *JCAP* **10**, 005, [arXiv:2204.12909 \[astro-ph.CO\]](#).
- [56] K. D. Lozanov and V. Takhistov, *Phys. Rev. Lett.* **130**, 181002 (2023), [arXiv:2204.07152 \[astro-ph.CO\]](#).
- [57] X.-B. Sui, J. Liu, and R.-G. Cai, *Phys. Rev. D* **111**, 123503 (2025), [arXiv:2412.08057 \[astro-ph.CO\]](#).
- [58] E. Cotner, A. Kusenko, and V. Takhistov, *Phys. Rev. D* **98**, 083513 (2018), [arXiv:1801.03321 \[astro-ph.CO\]](#).
- [59] E. Cotner, A. Kusenko, M. Sasaki, and V. Takhistov, *JCAP* **10**, 077, [arXiv:1907.10613 \[astro-ph.CO\]](#).
- [60] F. Muia, M. Cicoli, K. Clough, F. Pedro, F. Quevedo, and G. P. Vacca, *JCAP* **07**, 044, [arXiv:1906.09346 \[gr-qc\]](#).
- [61] Z. Nazari, M. Cicoli, K. Clough, and F. Muia, *JCAP* **05**, 027, [arXiv:2010.05933 \[gr-qc\]](#).
- [62] L. E. Padilla, J. C. Hidalgo, T. D. Gomez-Aguilar, K. A. Malik, and G. German, *Front. Astron. Space Sci.* **11**, 1361399 (2024), [arXiv:2402.03542 \[astro-ph.CO\]](#).
- [63] K. Kasai and N. Kitajima, (2025), [arXiv:2510.25300 \[astro-ph.CO\]](#).
- [64] M. A. G. Garcia, M. Pierre, and S. Verner, *Phys. Rev. D* **107**, 043530 (2023), [arXiv:2206.08940 \[hep-ph\]](#).
- [65] F. van Dissel, O. Pujolas, and E. I. Sfakianakis, *JHEP* **07**, 194, [Erratum: *JHEP* **04**, 191 (2025)], [arXiv:2303.16072 \[hep-th\]](#).
- [66] M. Gleiser, *Int. J. Mod. Phys. D* **16**, 219 (2007), [arXiv:hep-th/0602187](#).
- [67] G. Fodor, *A review on radiation of oscillons and oscillatons*, Ph.D. thesis, Wigner RCP, Budapest (2019), [arXiv:1911.03340 \[hep-th\]](#).
- [68] J. Ollé Aguilera, *On the Longevity, Quantum Decay and the role of Oscillons in Dark Matter*, Ph.D. thesis, Barcelona, Autonomia U. (2022).
- [69] S.-Y. Zhou, *Rept. Prog. Phys.* **88**, 046901 (2025), [arXiv:2411.16604 \[hep-th\]](#).
- [70] M. Gleiser and D. Sicilia, *Phys. Rev. Lett.* **101**, 011602 (2008), [arXiv:0804.0791 \[hep-th\]](#).
- [71] G. Fodor, P. Forgacs, Z. Horvath, and M. Mezei, *Phys. Rev. D* **79**, 065002 (2009), [arXiv:0812.1919 \[hep-th\]](#).
- [72] M. Gleiser and D. Sicilia, *Phys. Rev. D* **80**, 125037 (2009), [arXiv:0910.5922 \[hep-th\]](#).
- [73] M. P. Hertzberg, *Phys. Rev. D* **82**, 045022 (2010), [arXiv:1003.3459 \[hep-th\]](#).
- [74] K. Mukaida, M. Takimoto, and M. Yamada, *JHEP* **03**, 122, [arXiv:1612.07750 \[hep-ph\]](#).
- [75] M. Ibe, M. Kawasaki, W. Nakano, and E. Sonomoto, *JHEP* **04**, 030, [arXiv:1901.06130 \[hep-ph\]](#).
- [76] M. A. Amin and P. Mocz, *Phys. Rev. D* **100**, 063507 (2019), [arXiv:1902.07261 \[astro-ph.CO\]](#).
- [77] J. Ollé, O. Pujolàs, and F. Rompineve, *JCAP* **02**, 006, [arXiv:1906.06352 \[hep-ph\]](#).
- [78] H.-Y. Zhang, M. A. Amin, E. J. Copeland, P. M. Saffin, and K. D. Lozanov, *JCAP* **07**, 055, [arXiv:2004.01202 \[hep-th\]](#).
- [79] J. Olle, O. Pujolas, and F. Rompineve, *JCAP* **09**, 015, [arXiv:2012.13409 \[hep-ph\]](#).
- [80] D. Cyncynates and T. Giurgica-Tiron, *Phys. Rev. D* **103**, 116011 (2021), [arXiv:2104.02069 \[hep-ph\]](#).
- [81] M. Piani and J. Rubio, *JCAP* **12**, 002, [arXiv:2304.13056 \[hep-ph\]](#).
- [82] M. Piani, J. Rubio, and F. Torrenti, *JCAP* **06**, 024, [arXiv:2501.14869 \[hep-ph\]](#).
- [83] M. Drees and C. Wang, *JCAP* **04**, 078, [arXiv:2501.13811 \[astro-ph.CO\]](#).
- [84] S. Li, M. Yamaguchi, and Y.-l. Zhang, *JCAP* **12**, 028, [arXiv:2507.13276 \[hep-ph\]](#).
- [85] F. van Dissel and O. Pujolàs, *JHEP* **08**, 123, [arXiv:2505.00890 \[hep-th\]](#).
- [86] S. Li, (2025), [arXiv:2511.03501 \[hep-ph\]](#).
- [87] J. Evslin, K. Slawińska, T. Romańczukiewicz, and A. Wereszczyński, (2025), [arXiv:2512.17193 \[hep-th\]](#).
- [88] J. Garcia-Bellido and E. Ruiz Morales, *Phys. Dark Univ.* **18**, 47 (2017), [arXiv:1702.03901 \[astro-ph.CO\]](#).
- [89] J. M. Ezquiaga, J. Garcia-Bellido, and E. Ruiz Morales, *Phys. Lett. B* **776**, 345 (2018), [arXiv:1705.04861 \[astro-ph.CO\]](#).
- [90] H. Motohashi and W. Hu, *Phys. Rev. D* **96**, 063503 (2017), [arXiv:1706.06784 \[astro-ph.CO\]](#).
- [91] K. Kannike, L. Marzola, M. Raidal, and H. Veermäe, *JCAP* **09**, 020, [arXiv:1705.06225 \[astro-ph.CO\]](#).
- [92] G. Ballesteros and M. Taoso, *Phys. Rev. D* **97**, 023501 (2018), [arXiv:1709.05565 \[hep-ph\]](#).
- [93] O. Özsoy, S. Parameswaran, G. Tasinato, and I. Zavala, *JCAP* **07**, 005, [arXiv:1803.07626 \[hep-th\]](#).
- [94] M. Cicoli, V. A. Diaz, and F. G. Pedro, *JCAP* **06**, 034, [arXiv:1803.02837 \[hep-th\]](#).
- [95] S. S. Mishra and V. Sahni, *JCAP* **04**, 007, [arXiv:1911.00057 \[gr-qc\]](#).
- [96] K. Inomata, E. McDonough, and W. Hu, *Phys. Rev. D* **104**, 123553 (2021), [arXiv:2104.03972 \[astro-ph.CO\]](#).
- [97] K. Inomata, E. McDonough, and W. Hu, *JCAP* **02** (02), 031, [arXiv:2110.14641 \[astro-ph.CO\]](#).
- [98] A. Karam, N. Koivunen, E. Tomberg, V. Vaskonen, and H. Veermäe, (2022), [arXiv:2205.13540 \[astro-ph.CO\]](#).
- [99] B.-M. Gu, F.-W. Shu, K. Yang, and Y.-P. Zhang, *Phys. Rev. D* **107**, 023519 (2023), [arXiv:2207.09968 \[astro-ph.CO\]](#).

- [100] B.-M. Gu, F.-W. Shu, and K. Yang, *Phys. Dark Univ.* **47**, 101744 (2025), arXiv:2307.00510 [astro-ph.CO].
- [101] M. Y. Khlopov, *Res. Astron. Astrophys.* **10**, 495 (2010), arXiv:0801.0116 [astro-ph].
- [102] B. J. Carr, K. Kohri, Y. Sendouda, and J. Yokoyama, *Phys. Rev. D* **81**, 104019 (2010), arXiv:0912.5297 [astro-ph.CO].
- [103] B. Carr, M. Raidal, T. Tenkanen, V. Vaskonen, and H. Veermäe, *Phys. Rev. D* **96**, 023514 (2017), arXiv:1705.05567 [astro-ph.CO].
- [104] M. Sasaki, T. Suyama, T. Tanaka, and S. Yokoyama, *Class. Quant. Grav.* **35**, 063001 (2018), arXiv:1801.05235 [astro-ph.CO].
- [105] A. M. Green and B. J. Kavanagh, *J. Phys. G* **48**, 043001 (2021), arXiv:2007.10722 [astro-ph.CO].
- [106] B. Carr and F. Kuhnel, *Ann. Rev. Nucl. Part. Sci.* **70**, 355 (2020), arXiv:2006.02838 [astro-ph.CO].
- [107] B. Carr, K. Kohri, Y. Sendouda, and J. Yokoyama, *Rept. Prog. Phys.* **84**, 116902 (2021), arXiv:2002.12778 [astro-ph.CO].
- [108] P. Villanueva-Domingo, O. Mena, and S. Palomares-Ruiz, *Front. Astron. Space Sci.* **8**, 87 (2021), arXiv:2103.12087 [astro-ph.CO].
- [109] J. Auffinger, *Prog. Part. Nucl. Phys.* **131**, 104040 (2023), arXiv:2206.02672 [astro-ph.CO].
- [110] A. Escrivà, F. Kuhnel, and Y. Tada 10.1016/B978-0-32-395636-9.00012-8 (2022), arXiv:2211.05767 [astro-ph.CO].
- [111] M. Sasaki, T. Suyama, T. Tanaka, and S. Yokoyama, *Phys. Rev. Lett.* **117**, 061101 (2016), [Erratum: *Phys.Rev.Lett.* 121, 059901 (2018)], arXiv:1603.08338 [astro-ph.CO].
- [112] V. Vaskonen and H. Veermäe, *Phys. Rev. D* **101**, 043015 (2020), arXiv:1908.09752 [astro-ph.CO].
- [113] S. Clesse and J. Garcia-Bellido, *Phys. Dark Univ.* **38**, 101111 (2022), arXiv:2007.06481 [astro-ph.CO].
- [114] V. De Luca, G. Franciolini, P. Pani, and A. Riotto, *JCAP* **06**, 044, arXiv:2005.05641 [astro-ph.CO].
- [115] V. De Luca, V. Desjacques, G. Franciolini, P. Pani, and A. Riotto, *Phys. Rev. Lett.* **126**, 051101 (2021), arXiv:2009.01728 [astro-ph.CO].
- [116] M. Andrés-Carasona, A. J. Iovino, V. Vaskonen, H. Veermäe, M. Martínez, O. Pujolàs, and L. M. Mir, *Phys. Rev. D* **110**, 023040 (2024), arXiv:2405.05732 [astro-ph.CO].
- [117] C. Yuan, Z.-C. Chen, and L. Liu, *Phys. Rev. D* **112**, L081306 (2025), arXiv:2507.15701 [astro-ph.CO].
- [118] V. De Luca, G. Franciolini, and A. Riotto, (2025), arXiv:2508.09965 [astro-ph.CO].
- [119] P. Saha and Y. Urakawa, *JCAP* **04**, 061, arXiv:2412.17359 [astro-ph.CO].
- [120] F. Hasegawa and J.-P. Hong, *Phys. Rev. D* **97**, 083514 (2018), arXiv:1710.07487 [astro-ph.CO].
- [121] J. Kim and J. McDonald, *Phys. Rev. D* **105**, 063508 (2022), arXiv:2111.12474 [astro-ph.CO].
- [122] G. N. Felder, J. Garcia-Bellido, P. B. Greene, L. Kofman, A. D. Linde, and I. Tkachev, *Phys. Rev. Lett.* **87**, 011601 (2001), arXiv:hep-ph/0012142.
- [123] E. J. Copeland, S. Pascoli, and A. Rajantie, *Phys. Rev. D* **65**, 103517 (2002), arXiv:hep-ph/0202031.
- [124] R. Kallosh and A. Linde, *JCAP* **07**, 002, arXiv:1306.5220 [hep-th].
- [125] R. Kallosh, A. Linde, and D. Roest, *JHEP* **11**, 198, arXiv:1311.0472 [hep-th].
- [126] G. Floquet, *Annales scientifiques de l'École Normale Supérieure 2e série*, **12**, 47 (1883).
- [127] D. G. Figueroa, A. Florio, F. Torrenti, and W. Valkenburg, *JCAP* **04**, 035, arXiv:2006.15122 [astro-ph.CO].
- [128] D. G. Figueroa, A. Florio, F. Torrenti, and W. Valkenburg, *Comput. Phys. Commun.* **283**, 108586 (2023), arXiv:2102.01031 [astro-ph.CO].
- [129] J. Baeza-Ballesteros, D. G. Figueroa, A. Florio, J. Lizarraga, N. Loayza, K. Marschall, T. Opferkuch, B. A. Stefanek, F. Torrenti, and A. Urso, (2025), arXiv:2512.15627 [astro-ph.CO].
- [130] M. S. Turner, *Phys. Rev. D* **28**, 1243 (1983).
- [131] M. A. G. Garcia, K. Kaneta, Y. Mambrini, and K. A. Olive, *JCAP* **04**, 012, arXiv:2012.10756 [hep-ph].
- [132] A. R. Liddle and S. M. Leach, *Phys. Rev. D* **68**, 103503 (2003), arXiv:astro-ph/0305263.
- [133] J. F. Dufaux, A. Bergman, G. N. Felder, L. Kofman, and J.-P. Uzan, *Phys. Rev. D* **76**, 123517 (2007), arXiv:0707.0875 [astro-ph].
- [134] F. Li, N. Yang, Z. Fang, R. M. L. Baker, Jr., G. V. Stephenson, and H. Wen, *Phys. Rev. D* **80**, 064013 (2009), arXiv:0909.4118 [gr-qc].
- [135] T. Akutsu *et al.*, *Phys. Rev. Lett.* **101**, 101101 (2008), arXiv:0803.4094 [gr-qc].
- [136] A. S. Chou *et al.* (Holometer), *Phys. Rev. D* **95**, 063002 (2017), arXiv:1611.05560 [astro-ph.IM].
- [137] A. Patra *et al.*, *Phys. Rev. Lett.* **135**, 101402 (2025), arXiv:2410.09175 [gr-qc].
- [138] L. Pagano, L. Salvati, and A. Melchiorri, *Phys. Lett. B* **760**, 823 (2016), arXiv:1508.02393 [astro-ph.CO].
- [139] C. Caprini and D. G. Figueroa, *Class. Quant. Grav.* **35**, 163001 (2018), arXiv:1801.04268 [astro-ph.CO].
- [140] T. J. Clarke, E. J. Copeland, and A. Moss, *JCAP* **10**, 002, arXiv:2004.11396 [astro-ph.CO].
- [141] K. D. Lozanov, M. Sasaki, and J. Tränkle, (2026), arXiv:2601.11360 [astro-ph.CO].